Late Quaternary intraplate deformation defined by the Las Chacras Fault Zone, West-Central Argentina

Jeremy Rimando[1,2], Lindsay M. Schoenbohm[1,2], Gustavo Ortiz[3], Patricia Alvarado[3], Agostina Venerdini[3], Lewis A. Owen [4], Erin Seagren[1,2], Paula Marques Figueiredo[4], Sarah Hammer[5]

[1] Department of Earth Sciences, University of Toronto, Toronto, ON M5S 3B1, Canada
[2] Department of Chemical and Physical Sciences, University of Toronto Mississauga, Mississauga, Ontario L5L1C6, Canada
[3] Centro de Investigaciones de la Geósfera y la Biósfera (CIGEOBIO), Departamento de Geofísica y Astronomía, Facultad de Ciencias Exactas, Físicas y Naturales, Universidad Nacional de San Juan – Consejo Nacional de Investigaciones Científicas y Técnicas (CONICET), Meglioli 1160 S, Rivadavia, 5406, San Juan, Argentina
[4] Department of Marine, Earth, and Atmospheric Sciences, North Carolina State University, Raleigh, NC 27695, USA
[5] Department of Geology, University of Cincinnati, Cincinnati, OH 45221, USA

*Corresponding author: jeremy.rimando@mail.utoronto.ca

Abstract

Several major (up to M_W 7.5) earthquakes over the past 320 years have shaken the thick-skinned Sierras Pampeanas region of Argentina, despite exhibiting much lower GPS-shortening rates than across the thin-skinned Precordillera region to its west. Whether geodetic shortening rates indicate an actual long-term shortening gradient, and whether shortening rates translate to higher uplift rates due to steeper faults in the Sierras Pampeanas, remain uncertain due to the limited spatio-temporal coverage and the inherently large error in the vertical component of deformation of GPS measurements. We measure geomorphic offsets and use ^{10}Be terrestrial cosmogenic nuclide surface exposure dating to determine slip rates on the Las Chacras Fault Zone (LCFZ)—an ~30 km long, NNW-trending, steeply-dipping (55 to 65°E) reverse fault that branches off of the longest, westernmost, thick-skinned Valle Fértil range-front fault in the western Sierras Pampeanas. Average shortening and uplift rates measured on the LCFZ are ~0.2 and ~0.3–0.4 mm/yr, respectively. Despite an uplift rate similar to most other faults in the region, the LCFZ shortening rate is lower than faults to its west; this is in agreement with the inferred west-east decrease in shortening rates from GPS data, indicating consistent regional deformation patterns since the Late Pleistocene. The decrease in shortening to the east coincides spatially with the termination of the flat portion of the subducted Nazca plate between 67 and 68°W. From scaling relationships among magnitude, slip rate, and fault length, the LCFZ is capable of generating earthquakes of M_W 6.7–7.1.

1. Introduction

Quaternary Andean backarc deformation within the Pampean segment (27–33.5°S) related to the convergence of the Nazca and South American plates is

This article has been accepted for publication and undergone full peer review but has not been through the copyediting, typesetting, pagination and proofreading process, which may lead to differences between this version and the Version of Record. Please cite this article as doi: 10.1029/2020TC006509.

widely distributed, extending up to 700 km east from the Perú-Chile trench (**Fig. 1A)**. The plate margin encompasses the thin-skinned fold-and-thrust belts of the Andean Main Cordillera, Frontal Cordillera, and Precordillera in the west, and the thick-skinned reverse faults of the Sierras Pampeanas in the east (**Fig. 1B**). This wide distribution and partitioning of deformation among structures with different tectonic styles has been associated with subduction of a shallowly dipping section of the Nazca plate at these latitudes, known as the Pampean flat-slab segment (**Fig. 1B**; Ramos, 1988; Ramos, 1999; Ramos et al., 2002; Ramos et al., 2004; Ramos & Folguera, 2009; Ammirati et al., 2015, 2018).

Since ~20 Ma, bivergent, thin-skinned fold-and-thrust orogenic belts (Armijo et al., 2010; Riesner et al., 2018) in the retroarc region of the Pampean flat-slab segment have accommodated most of the permanent shortening between the plate boundary and the forearc region (Baby et al., 1997; Zapata & Allmendinger, 1996; Fosdick et al., 2015). In the past 10–15 Ma, up to ~75% of this total shortening at 30°S has been accommodated in the thin-skinned orogenic belts of the Precordillera (Allmendinger et al., 1990; Levina et al., 2014; Fosdick et al., 2015). Between 30 and 32°S**,** activity in the easternmost Precordillera that commenced at ~2.6 Ma and in the westernmost Sierras Pampeanas at ~3 Ma (Jordan et al., 1993; Costa, 2019) has focused deformation between these two sections of the retroarc, forming the Andean Orogenic Front (AOF; **Fig. 1B**).

Compared to the thin-skinned structures in the west (e.g., Las Peñas, La Rinconada and Las Tapias faults, **Fig. 1**; Siame et al., 2002; Costa et al., 2019, and references therein; Rimando et al., 2019), little is known about the rates of movement of most of the basement-cored uplifts of the Sierras Pampeanas. These structures create significant relief in the retroarc region of Argentina (Costa, 2019). GPS studies covering observations from 1993 to 2001 demonstrate that shortening rates decrease from west to east (Brooks et al., 2003; Kendrick et al., 2003), suggesting low shortening rates for Pampean structures. However, whether this trend holds true on the longer term is unclear due to the sparseness of observation points, poor vertical positional accuracy, and limited temporal coverage of GPS data. In order to build a picture of long-term deformation across the Pampean flat-slab segment, we focus on the Las Chacras Fault Zone (LCFZ; labelled '23' in **Fig. 2**), which is a key regional structure considering fault length, evidence of recent morphologic displacement, significant instrumental seismicity, and proximity of the LCFZ to structures that have been associated with generation of major earthquakes (**Figs. 2 & 3**).

This study presents the first terrestrial cosmogenic nuclide (TCN) dating-based Quaternary slip rate measurements along the Pan de Azúcar strand of the LCFZ (**Fig. 3**), and the only other geomorphic slip rate study on thick-skinned Pampean fault scarps aside from the Pajaritos Fault (Northern Pie de Palo) (Siame et al., 2015). Investigating slip rates along the LCFZ provides a good opportunity to understand how much shortening and uplift occurs on thick-skinned, intraplate structures relative to thin-skinned, plate boundary-related structures on a longer timescale (up to Late Pleistocene). Our study also allows us to estimate possible earthquake magnitudes, which proves challenging not only in the Sierras

Pampeanas, but in any intraplate setting (McCalpin, 2009) due to the rarity of well-preserved scarps resulting from long recurrence intervals on slow-moving faults (Stein, 2007). Similar to the 1977 M_w 7.5 Caucete (San Juan, Argentina) earthquake of the western Sierras Pampeanas, which involved motion along the adjacent Ampacama-Niquizanga fault (Bastías, 1985; Volponi et al., 1978; Kadinsky-Cade et al., 1985; Langer & Hartzell, 1996) (**Fig. 2**), an earthquake with magnitude greater than ≥7 generated by the LCFZ could potentially cause damage to nearby smaller towns and cities in San Juan Province (**Fig. 2**) and could be felt as far away as Buenos Aires (~900 km away) (Alvarado et al., 2020).

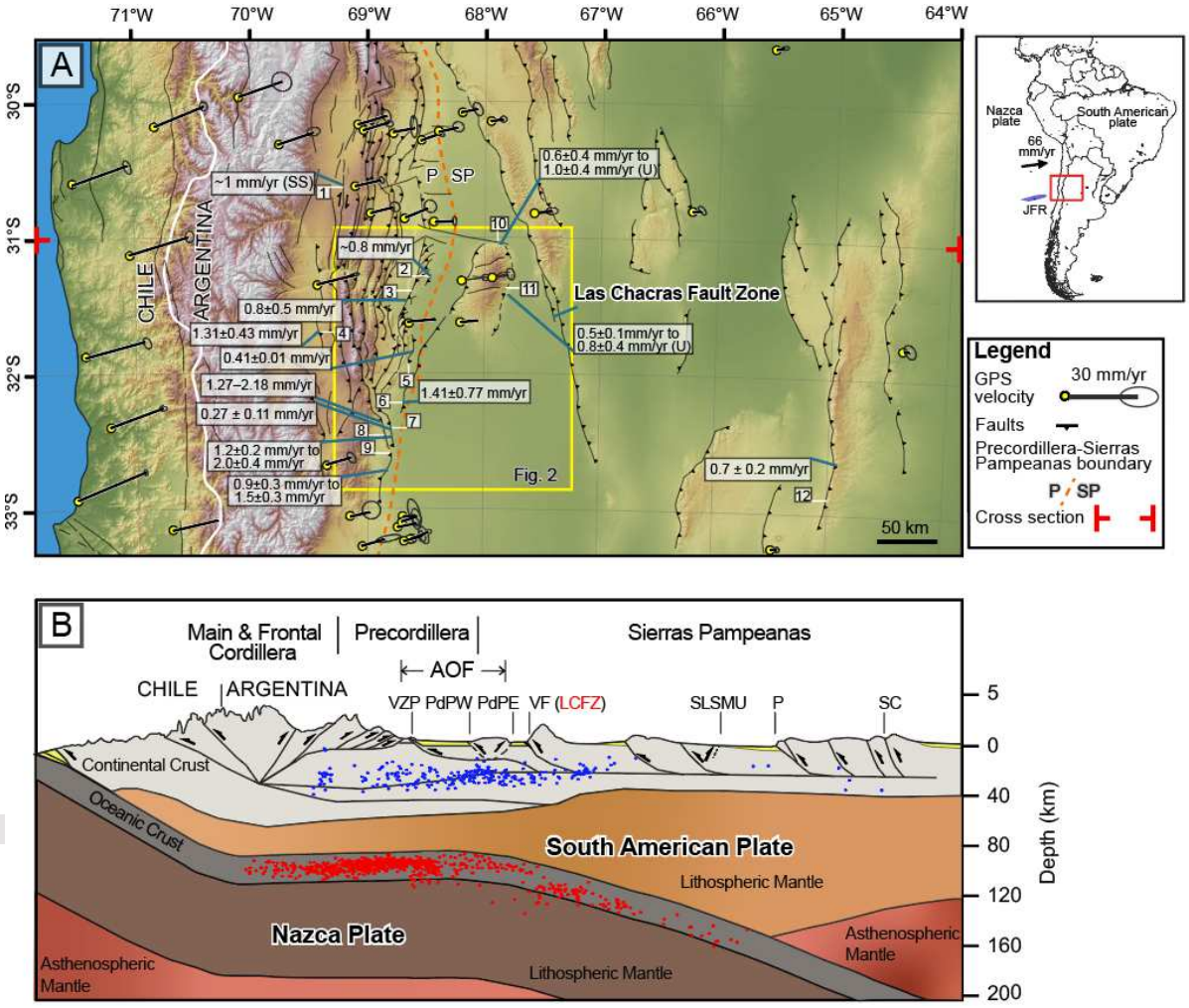

Figure 1. A. Map showing tectonic features (Costa et al., 2000; Siame et al., 2002), GPS velocity uncertainty ellipses (Brooks et al., 2003), and Quaternary slip rates (Costa et al. 2015a&b; Costa et al., 2018; Costa et al., 2019; García Morabito et al., 2020; Rimando et al., 2019; Rockwell et al., 2014; Salomon et al., 2013; Schmidt, et al., 2011a; Siame et al., 1997, 2002, 2006, 2015) in the Pampean flat-slab segment of the Central Andes. Numbers in white boxes indicate faults with known Quaternary slip rates (shortening rates except for those followed by the letter 'U', which correspond to uplift rates): 1—El Tigre (strike slip SS) Fault, 2—La Laja Fault, 3—Las Tapias segment of Villicum-Zonda-Pedernal Thrust, 4—Barreal Fault, 5—La Rinconada Fault Zone, 6—Cerro Salinas Fault 7—Las Peñas Thrust, 8—Las Higueras Thrust, 9—La Cal Thrust, 10—Northern Sierra Pie de Palo (Pajaritos) Fault, 11—Eastern Sierra Pie de Palo Fault, and 12—Los Molinos branch of the Comechingones Fault. Vector indicating the GPS velocity of the Nazca plate with respect to the South

American plate and the location of the Juan Fernández Ridge (JFR) are indicated in the inset. B. Schematic cross section through 31°S to 31.5°S showing the geometry of predominantly thin-skinned structures in the Cordillera and Precordillera regions and thick-skinned structures of the Sierras Pampeanas region (modified from Ramos et al., 2002) and the geometry of the subduction Nazca plate at 30-31°S (Ammirati et al., 2015). Well-localized seismicity in the Argentinian side of the flat slab are from the following sources: Linkimer et al.'s (2020) two temporary seismological networks, the SIEMBRA (SIerras Pampeanas Experiment using a Multicomponent BRoadband Array; Beck & Zandt, 2007) between 2007 and 2009, and the ESP (Eastern Sierras Pampeanas) array between 2008 and 2010 (Gilbert, 2008); blue and red circles indicate overriding plate and subducting slab seismicity, respectively. AOF—Andean orogenic front, VZP—Villicum-Zonda-Pedernal Fault, PdPW—Western Pie de Palo Fault, PdPE—Eastern Pie de Palo, VF—Valle Fértil Fault, LCFZ—Las Chacras Fault Zone, SLSMU—Sierras de Los Llanos, Sierras de las Minas and Ulapes Fault, P—Pocho Fault, SC—Sierra Chica Fault Zone (modified from Rimando et al., 2019).

2. Background

2.1. Regional tectonic setting

Subduction of the oceanic Nazca plate beneath the continental South American plate along the Perú-Chile trench gave rise to the ~7000-km-long Andes Mountain range, with elevations of more than ~6900 m above sea level (asl) between 27 and 33°S. At the latitudes of South-Central Andes, where maximum crustal shortening and thickening are observed (Isacks, 1988; Kley & Monaldi, 1998; Arriagada et al., 2008; Chulick et al., 2013; Schepers et al., 2017), deformation extends further into the interior of the overriding plate. In particular, within the Pampean flat-slab segment (27–33°S), which is characterized by nearly horizontal subduction (**Fig. 1B;** Cahill & Isacks, 1992; Engdahl et al., 1998; Jordan et al., 1983a&b; Ramos, 1999; Gans et al., 2011; Ammirati et al., 2015), deformation reaches as far as 700 km east of the Chilean Trench (Richardson et al., 2013). Subduction of the aseismic Juan Fernández Ridge has been suggested as one of main factors responsible for shallowing of the Nazca plate between 27 to 33°S (Nur and Ben-Avraham, 1981; Pilger, 1984; Gutscher et al., 2000; Portner et al., 2017). Propagation of deformation into the foreland is facilitated by increased interplate coupling between the shallowly subducting Nazca plate and the overriding South American plate and/or by thermal weakening resulting from the eastward shift of arc magmatism (Kay et al., 1991; Yáñez et al., 2001; Ramos et al., 2002).

The Sierras Pampeanas are characterized by nearly north-south oriented, thick-skinned Precambrian to early Paleozoic crystalline basement-cored uplifts that comprise the intraplate deformation observed in the Pampean flat-slab segment (González Bonorino, 1950). These block uplifts exhibit asymmetric topographic profiles, with steeper fault-bounded sides contrasting with gentler preserved erosional surfaces on their other sides, a morphology which is indicative of listric fault geometry (Jordan & Allmendinger, 1986). The active deformation occurring within the Sierras Pampeanas, which is controlled mainly by pre-existing zones of weakness such as Mesozoic rift structures (Schmidt et al., 1995; Ramos et al., 2002) and sutures between terranes accreted to western Gondwana (Alvarado et al., 2009), is likely a modern analogue of the late Mesozoic-Early Cenozoic Laramide

orogeny in western North America (Jordan et al., 1983; Jordan & Allmendinger, 1986; Ramos et al., 2002).

GPS observations indicate a modern plate convergence rate of ~63 mm/yr at the latitudes of the Pampean flat-slab segment (Brooks et al., 2003; Kendrick et al., 2003). In the retroarc, horizontal velocity vectors suggest shortening rates that are an order of magnitude lower, but with highly localized strain. Much of this strain is focused in a zone of localized deformation in the retroarc, which lies between the Eastern Precordillera and the Western Sierras Pampeanas, called the active Andean Orogenic Front (AOF; **Fig. 1B**; Brooks et al., 2003; Costa, 1999; Fielding and Jordan, 1988; Groeber, 1944; Kadinsky-Cade et al., 1985; Meigs et al., 2006; Ramos et al., 1997; Siame et al., 2002, 2005, 2015; Smalley et al., 1993; Uliarte et al., 1987; Vergés et al., 2007; Alvarado et al., 2005). Shortening rate estimates from GPS studies within the AOF range from 2 to 7 mm/yr (Kendrick, et al., 1999, 2001, 2003, 2006; Brooks et al., 2003). GPS velocities are best explained by a model in which the AOF behaves as the eastern boundary of an Andean block situated in between the Nazca and South American plates (Brooks et al., 2003). The AOF is also characterized by crustal seismicity that correlates well with geomorphic evidence of Late Quaternary deformation (Cahill and Isacks, 1992; Engdahl et al., 1998; Gutscher et al., 2000; Smalley et al., 1993; Alvarado et al., 2005).

The Sierras Pampeanas of western Argentina are one of the most seismically active regions of thrust tectonics worldwide (Gutscher, 2002). Crustal seismicity is characterized by high levels of earthquake activity with hypocentral depths ranging from 10 to 35 km (Smalley & Isacks, 1990; Alvarado et al., 2005). In the past three centuries, the Argentine provinces of San Juan and Mendoza were shaken by damaging earthquakes (**Fig. 2**) that occurred along Precordilleran structures (Smalley & Isacks, 1990; Smalley et al., 1990, 1993; Engdahl & Villaseñor, 2002; Alvarado et al., 2007). The 1861 M>7 Mendoza earthquake may have occurred along the Las Higueras Thrust (Mingorance, 2006). The 1944 M_W 7.0 San Juan earthquake was generated along the La Laja fault system (Castellanos, 1944; Groeber, 1944; Harrington, 1948; Alvarado & Beck, 2006). The 1952 M_W 6.8 San Juan earthquake was possibly generated along the La Rinconada Fault (Alvarado & Beck, 2006; Rimando et al., 2019, and references therein). Finally, the January 18, 2021 M_W 6.4 San Juan earthquake, whose detailed seismic source and associated structure has yet to be determined (USGS, 2021). However, historical earthquake records associated with Pampean structures are scarce, with no documented large magnitude earthquakes in the Western Sierras Pampeanas except for the 1977 M_W 7.4 Caucete earthquake (**Fig. 2**). Several studies have linked this event to the Ampacama-Niquizanga Fault (Volponi et al., 1978; Bastías, 1985; Kadinsky-Cade et al., 1985; Langer & Hartzell, 1996). Evidence of coseismic ground ruptures, rock avalanches and liquefaction effects that suggest large magnitude prehistoric earthquakes along or adjacent to faults in the Sierras Pampeanas (Costa et al., 2018, and references therein), however, indicate that intraplate faults in the Sierras Pampeanas region could be more active and pose a larger seismic hazard than previously thought (Costa et al., 2018, and references therein).

2.2. Las Chacras Fault Zone

The LCFZ (**Figs. 2, 3, 4 & 5**) is aligned with the southern end of the ~180-km-long Valle Fértil Fault (VFF), a similarly east-dipping (40–45°) thrust fault system on the western flank of the Valle Fértil-La Huerta range (**Fig. 3 & 6**; Furque et al., 1998; Ragona et al., 1995; Ramos & Vujovich, 2000; Vujovich et al., 1998; Ortiz et al., 2015). The fault-bounded mountain range is composed of a Proterozoic igneous and metamorphic basement complex overlain by Triassic sedimentary rocks (**Figs. 3 & 6**). The seismically active Valle Fértil Fault has accommodated backarc contractional deformation since the Miocene (Brooks et al., 2003; Fosdick et al., 2015; Ortiz et al., 2015; Japas et al., 2016). This structure also delimits the Famatinian suture (Ramos, 1994), which exhibits ductile deformation and accommodation of extensional deformation during Triassic and Cretaceous times (Jordan & Allmendinger, 1986; Uliana et al., 1989; Ramos, 1994; Rossello & Mozetic, 1999). The Valle Fértil Fault carries Proterozoic basement rocks over the Cenozoic foreland strata of the Bermejo basin (Snyder et al., 1990; Zapata & Allmendinger, 1996). Ortiz et al. (2015) documented a trend of deformation that youngs toward the northern and southern tips of the Valle Fértil-La Huerta range since the Pliocene from thermochronological dating. Ortiz et al. (2015) noted a correlation between locations of Quaternary deformation with middle to lower crustal seismicity along the northern and southern portions of the Valle Fértil-La Huerta range (e.g., Kadinsky-Cade et al., 1985), which suggests a consistency in the deformation pattern from the Pliocene to the present.

The LCFZ (**Figs. 2 & 3**), on the southwestern piedmont of the Sierra de Valle Fértil-La Huerta Range, is a northwest-southeast trending, ~30-km-long, 60°E-dipping zone of reverse faults located ~100 km east of the city of San Juan in Argentina (Pérez et al., 1997; Costa et al., 2000). Two main fault strands comprise the LCFZ: the Pan de Azúcar Fault (PAF) in the west and the Rickard Fault (RF) in the east. Approximately 20-m-high, west-facing downslope-directed, cumulative displacement scarps of the Pan de Azúcar Fault cut through three well-preserved alluvial fan and strath terrace surfaces (Q1, Q2 and Q3) at several locations (**Fig. 3**). In contrast, the < 5-m-high scarps of the Rickard Fault cut only through a few poorly preserved Q2 alluvial surfaces. For these reasons, we conducted our study on the prominent cumulative scarps of the Pan de Azúcar fault strand (**Figs. 2, 3, 4 & 5**) where conditions are suitable for determining short- and long-term slip rates through terrestrial cosmogenic nuclide (TCN) surface exposure dating and measurement of fault offset. At the southern tip of the range, Rothis et al. (2018) reported Quaternary alluvial surfaces offset by the LCFZ (**Fig. 3**); Rothis et al. (2019) measured slip rates by optically stimulated luminescence (OSL) dating of some displaced alluvial deposits.

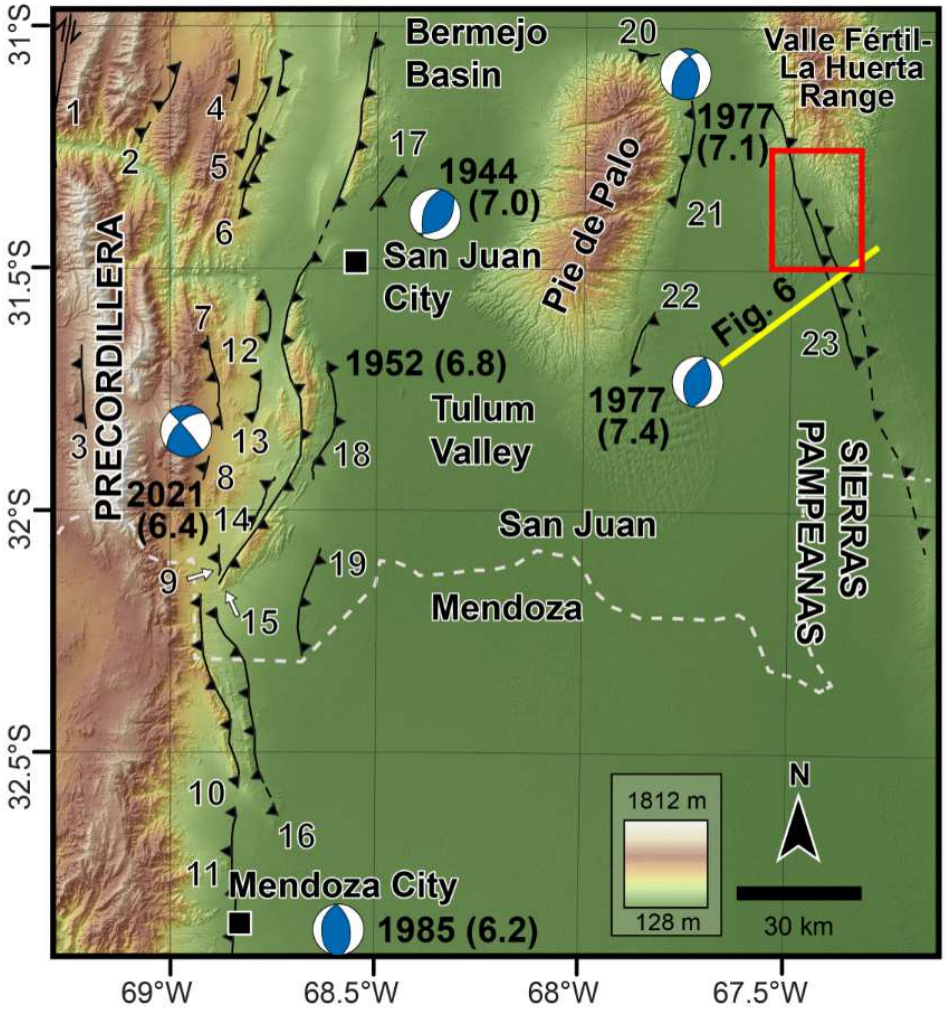

Figure 2. Quaternary-active faults and focal mechanisms (FM) of large crustal earthquakes near San Juan and Mendoza, Argentina (Alvarado & Beck, 2006; Langer & Hartzell, 1996; USGS 2021). The red box shows the location of Figure 3 and the broken white line indicates the boundary of the provinces of San Juan and Mendoza. The late Quaternary faults are: 1—El Tigre, 2—La Cantera, 3—Ansilta-Jarillal, 4—Los Gauchos, 5—Dehesa, 6—Blanquitos, 7—Maradona, 8—Las Osamentas, 9—Acequión, 10—Las Higueras, 11—La Cal, 12—Cerro Zonda, 13—Papagallos, 14—Cerro La Chilca, 15—Villicum-Zonda-Pedernal, 16—Las Peñas, 17—La Laja, 18—La Rinconada, 19—Cerro Salinas, 20—Northern Sierra Pie de Palo (Pajaritos), 21—Ampacama, 22—Niquizanga, and 23—Las Chacras (Costa et al., 2000; Perucca & Vargas, 2014; https://sara.openquake.org/; and http://sigam.segemar.gov.ar/visor/).

3. Methods

3.1. Geologic and geomorphic mapping

We compiled structural, geologic, and geomorphic data gathered in the field on high-resolution satellite images from Microsoft Bing Maps (https://www.bing.com/maps) and 30-m-resolution Advanced Spaceborne Thermal Emission and Reflection Radiometer (ASTER) global digital elevation models (GDEM) (https://asterweb.jpl.nasa.gov/gdem.asp).

We made a 1:50,000 scale geologic map of the vicinity of the LCFZ by integrating our field observations with previous work (**Fig. 3**). We also produced a 1:10,000 scale geomorphic maps of the fault-offset geomorphic landforms (alluvial fans and strath terraces) for three sites: the El Arenal, Quebrada del Barro, and El Carrizal (**Figs. 3, 4, 7 & 8**). Identification of different alluvial fans and strath terraces was guided by stratigraphic relationships, surface morphology, and weathering characteristics using methods similar to those of McFadden et al. (1989) and Owen et al. (2014). Surfaces were labelled 'Q' for Quaternary followed by a number ('1' being the oldest).

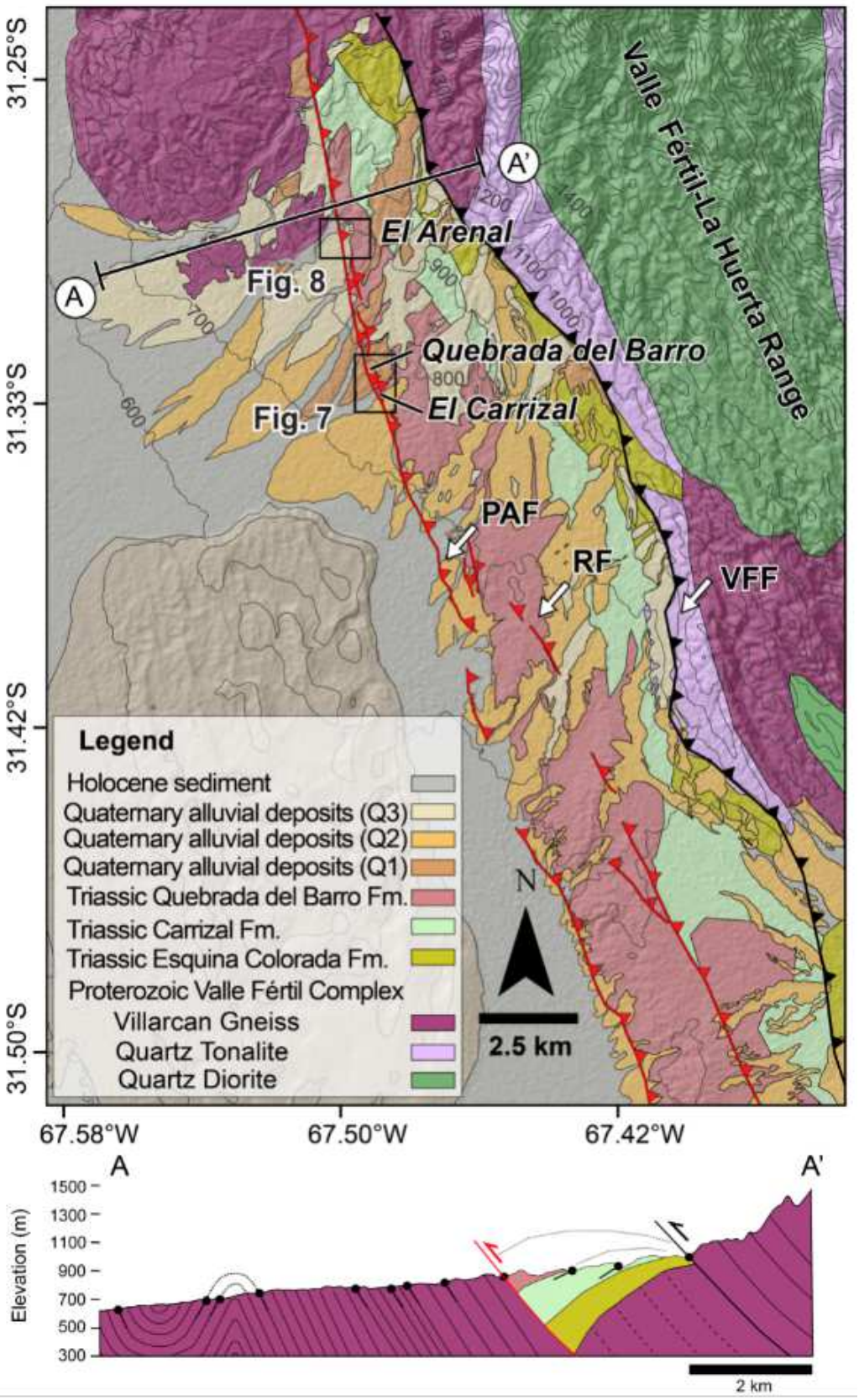

Figure 3. Geologic map and cross section across the Pan de Azúcar strand of the Las Chacras Fault Zone (red outline indicates late Quaternary activity) and the Valle Fértil Fault (Ragona et al., 1995; Furque et al., 1998; Vujovich et al., 1998; Ramos & Vujovich, 2000; Ortiz et al., 2015; Rothis et al., 2019). PAF—Pan de Azúcar Fault, RF—Rickard Fault, VFF—Valle Fértil Fault. Lines extending from 'El Carrizal' and 'Quebrada del Barro' point to locations of figures 4A and 4B, respectively. Topographic contour values are in meters.

3.2. ^{10}Be cosmogenic nuclide surface exposure dating

We employed ^{10}Be TCN surface exposure dating (Lal, 1988, 1991; Gosse & Phillips, 2001) combined with measurements of displacement on fault scarps to calculate average slip rates along the LCFZ.

We assume that ^{10}Be is produced primarily through spallation reactions with oxygen and silicon in quartz (Brown et al., 1989, 1992). Considering ^{10}Be production rate, altitude, latitude, changes in the geomagnetic field, topographic shielding, minimal or known erosion rate, and measured concentrations of ^{10}Be in surface samples, it is possible to estimate surface exposure ages (Gosse & Phillips, 2001). We apply this methodology to the silicate-rich alluvial fans and strath terraces of the El Arenal, Quebrada del Barro, and El Carrizal sites (**Fig. 3; supplementary figures S1-S5**).

To estimate surface exposure ages, we collected silicate-rich surface clasts. We also collected two depth profiles from the Q1 and Q2 surfaces (**supplementary figures S6A&B)**. Unfortunately, in both depth profiles, several samples with sediment that ranged in size from sand (0.25–1 mm) to granule-pebble (2–10 mm) yielded insufficient amounts of quartz with less than 300 ppm of Al_2O_3 (which is the suggested upper limit of Al_2O_3 for best Be precipitation laboratory procedure) (e.g., Stone, 2001). Inductively coupled plasma optical emission spectrometry (ICP-OES) analysis revealed significant silicate inclusions rich in alumina (Al_2O_3) in the quartz we collected. For this reason, we only used surface clasts for determining surface exposure ages.

Given the scarcity of boulders in the alluvial fan surfaces at the sites we investigated, we collected cobbles. Cobbles are preferable to finer sediments, as the age estimates from cobbles are not as prone to water and biogenic disturbance (Schmidt et al., 2011b; Ivy-Ochs et al., 2013; Tranel & Strow, 2017) and grain size dependency on cosmogenic nuclide concentrations (Belmont et al., 2007; Carretier et al., 2015; van Dongen et al., 2019; Lukens et al., 2016).

We collected flat, quartz-rich surface cobbles (~15-cm-diameter, ~4-cm-thickness) from the alluvial fan surfaces and active channels (**Figs. 7 & 8**). We gathered 30 clasts each from Q2, Q3, Q4 and the active channels in El Arenal and El Carrizal sites for amalgamation. Flat cobbles were chosen to ensure that most of the clast has been uniformly exposed to cosmic rays. We collected one set of amalgamated clasts per site, since ages from amalgamated cobble-sized samples were originally intended to corroborate ages from depth profiles.

Amalgamated surface cobbles have been widely used to measure alluvial surface exposure ages (e.g., Anderson et al., 1996; Repka et al., 1997; Hetzel et al., 2002) since these are thought to approximate the timing of alluvial fan surface abandonment despite the presence of some amount of inherited nuclide concentration (e.g., Brown et al., 1998; Riihimaki et al., 2006; Matmon et al., 2009). Typically, ~30 clasts are collected to statistically average out possible preexposure nuclide concentration outliers (Anderson et al., 1996; Repka et al., 1997).

To account for inheritance, which is likely in clasts from alluvial surfaces (e.g. Lal, 1991; Anderson, et al., 1996; Repka et al., 1996; Blisniuk et al., 2012; Brocard et al., 2003), we subtract the average nuclide concentrations of clasts taken from the active channel from the nuclide concentration of the clasts from the alluvial surface. This is done under the assumption that long-term erosion rates have not changed significantly since the alluvial surfaces were formed, and therefore provide a good proxy for the cosmogenic nuclide concentration produced by prior exposure at the sediment source area and during transport (e.g., Brown et al., 1998; Hancock et al., 1999; Hetzel et al., 2002; González et al., 2006; Machette et al., 2008; Armstrong et al., 2010; Le Dortz et al., 2011; Owen et al., 2011; Dühnforth et al., 2017). Nonetheless, we test the effects of assuming various erosion rates and inheritance scenarios in section 4.1.2 to to calculate a range of plausible ages, and consequently, slip rate estimates.

Data for all samples is presented in Table 1. All samples were processed at the Cosmogenic Nuclide Laboratories at the University of Cincinnati, USA, following standard methods (Kohl & Nishiizumi, 1992). After both crushing and amalgamating samples, we isolated quartz from the 250–500 μm size range through magnetic separation, acid leaches (aqua regia, 5% HF/HNO_3), frothing, and LST (lithium heteropolytungstate) heavy liquid separation. Samples were tested with ICP-OES (induced coupled plasma-optical emission spectrometry) to ensure low Al_2O_3 content. Final, clean quartz samples ranged between ~7 and 20 g. We added ~0.35 g of ^{9}Be carrier (provided by Abaz Alimanovic of the University of Melbourne, Australia) to each sample and three chemical blanks. After removing Fe, Ti, and Al, we precipitated $Be(OH)_2$ and converted it to BeO through ignition. We then mixed the resulting BeO with Nb powder (2:1 Nb:BeO) and loaded the mixture into stainless steel targets for AMS analysis at PRIME Lab at Purdue University, USA.

To calculate the topographic shielding for the different sampling sites, we used the version 2 of the topographic shielding calculator (http://stoneage.ice-d.org/math/skyline/skyline_in.html; last accessed July 2020). We then computed surface ages using the ^{10}Be version 3 code of the online exposure age calculator by Balco et al. (2008), formerly known as the CRONUS-Earth online exposure age calculator (https://hess.ess.washington.edu/math/v3/v3_age_in.html; last accessed July 2020), using the 'Lal/Stone' time-dependent (Lm) scaling scheme (Lal, 1991; Stone, 2000). We prefer to use the "Lm" scaling scheme as this accounts for production rate flux due to temporal variations in the geomagnetic field. Information used for age calculation can be found in Table 1.

We also collected four individual clasts from Q2 for analysis to test the internal consistency of amalgamated clast ages using Kernel Density Estimation (**Fig. 9**). We independently computed ages of these clasts on version 3 of the online calculators by Balco et al. (2008), plotting them as kernel density estimates (estimates for the probability density function) using iceTEA (Tools for Exposure Ages), an online set of tools for visualizing and analyzing cosmogenic-nuclide surface-exposure data principally from past ice margins by Jones et al. (2019) (http://ice-tea.org/en/; last accessed July 2020). The iceTEA plotter allowed us to visually evaluate the age

distribution of clasts and calculate a weighted mean age for the samples following an approach described in Jones et al. (2019).

3.3. Scarp topographic profiling with differential global positioning system (DGPS) surveys

We conducted millimetric-precision topographic surveys using a Trimble® R3 DGPS PPK (post-processed kinematic) survey system to construct fault scarp profiles (**Fig. 10A-D**). The setup includes both a base station and two rover units that record both raw positional information and positional correction data.

We surveyed alluvial and strath terrace surfaces cut by the Pan de Azúcar strand of the LCFZ at the El Arenal, Quebrada del Barro, and El Carrizal sites. We transited the fault scarps orthogonally, holding the rover units at a fixed height above the ground. These data were corrected with data from a base station. We approximate regional slope of the surface by extending the survey at least ~50 m on either side of the scarps.

We used Trimble® Business Center 2 to perform post-processing of positional information and positional correction data. We then used the point profile interactive tool on ESRI's desktop application, ArcMap, to construct the scarp profiles from the discrete survey points.

3.4. Displacement calculation

We measured displacement on scarps by solving equations from Yang et al. (2015) based on geometric relations among lines representing the displaced surfaces and the fault. This approach requires as input: slope (m) and y-intercept (b) values from linear regressions of hanging wall, footwall, and scarp surface survey points; fault dip; and fault-tip x-axis position. Although this approach accounts for the differences in the inclination of the hanging wall and footwall surfaces it assumes that the fault plane and the hanging wall and footwall surfaces are perfect planes (**Fig. 10E**). We used a fault dip of 60°E based on measurements of fault exposures in our study area (**Fig. 5**) and assumed a fault-tip position at the base of each scarp for calculation of displacement on all fault scarps. While there are no visible offset markers on the mesoscopic sectional view of the major strands of the Pan de Azúcar fault, exposures adjacent to the major fault strands show similarly steep reverse fault displacement on minor fault traces within the fault zone. These faults appear to follow the structural fabric of a pre-existing, steeply-dipping "shear zone" also documented by Rothis et al. (2019).

We analyzed an oil-industry seismic reflection profile from the *Energía Provincial Sociedad del Estado* (EPSE), Government of San Juan that runs across the western Sierras Pampeanas and captures the dips of the structures at depth (**Fig. 6**). We used MOVE™ software by Petroleum Experts Limited (https://www.petex.com/), which includes depth conversion among other options, to interpret the seismic profile. We assume an average seismic velocity V_0 of 2500 m/s for the dominantly-sandstone Cenozoic sedimentary package of the Bermejo Basin

on the Western Precordillera (Beer and Jordan, 1988; Snyder et al., 1990); 3500 m/s for the coarse-grained sandstone Mesozoic deposits that are manifested in the western sector of the Sierra de Valle de Fértil-La Huerta range (Snyder et al., 1990); and 6000 m/s for the gneissic basement (Snyder et al., 1990). Faults were delineated by recognizing offset in the traced reflectors. Since this seismic profile is oriented slightly oblique to the fault trend, the dips measured from the seismic reflection profiles are apparent, and on average are 5° steeper in reality. Therefore, most of the faults exhibit true dips at depth that range from 40-45°E. Towards the northeast of the seismic profile, in the area where the PAF and RF strands of the LCFZ; and the VFF are expected, the reflectors become unclear. However, it is likely that at depth these faults follow similar dips as the faults further west, and then emerge closer to the surface (at less than ~1 km) at steeper dips of ~60°E (as observed in outcrops).

We used a Monte Carlo simulator for propagation of uncertainties (Murphy, 2013) requiring the displacement equation and input parameter values along with their corresponding distribution types and uncertainties. All of the input parameters were characterized by a normal distribution, with the exception of the fault-tip x-axis position, which followed a uniform distribution. For 1-sigma uncertainty values of fault dip and the x-axis position of the fault tip, we used ± 5° and ± 1 m, respectively. For uncertainty associated with the slope and y-intercept values of the hanging wall, footwall, and scarp surface regressions, we derived values from the linear regression statistics. We computed shortening and uplift from the dip-slip component of displacement using the dip of the fault measured at the surface. We ran the model for 10000 iterations.

Figure 4. Profile views of the Pan de Azúcar strand of the LCFZ. A. Scarps at the El Carrizal site where Q2 is displaced. B. Scarps at the Quebrada del Barro site where Q1 is displaced. Locations are indicated with labels on Fig. 3.

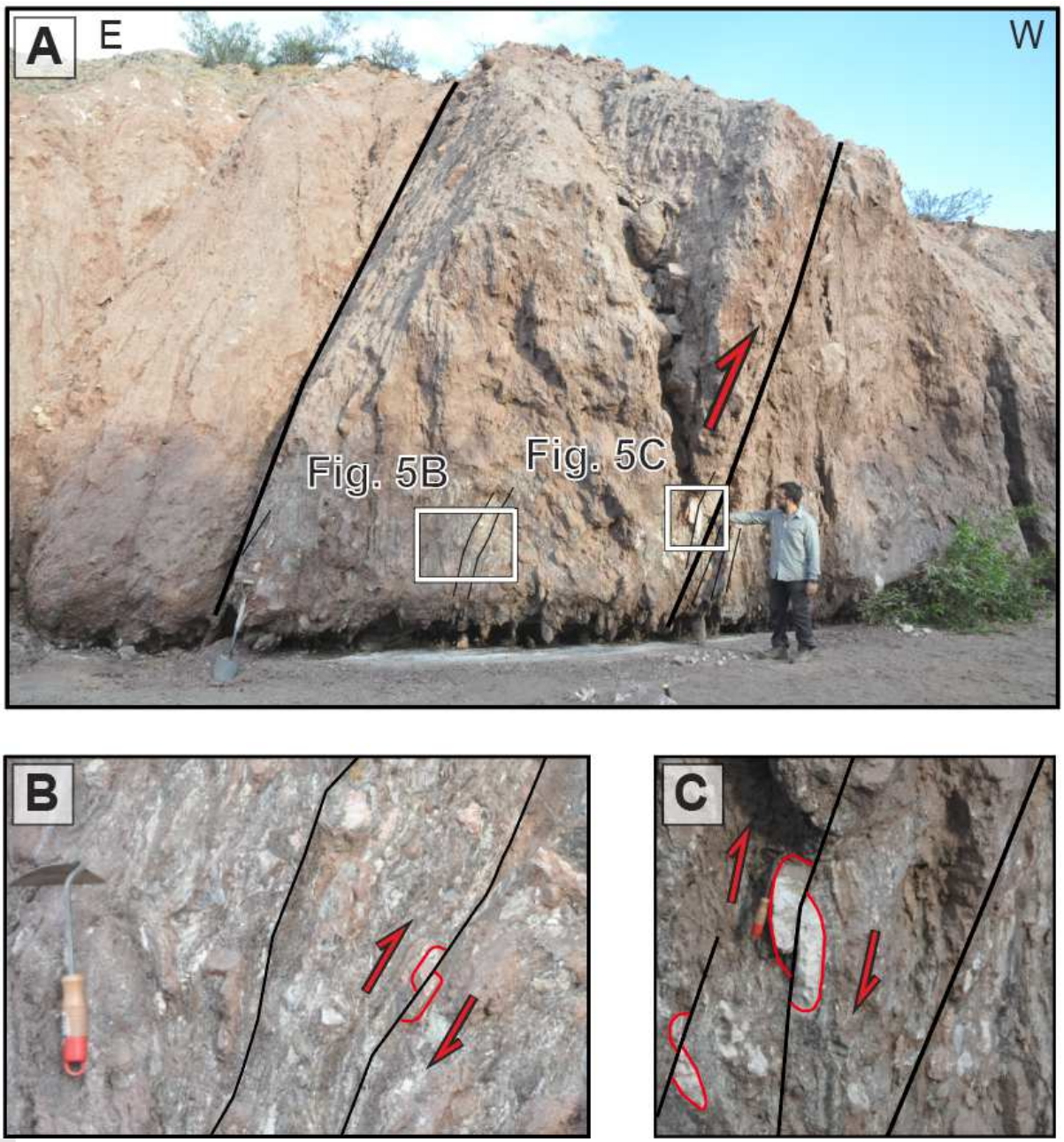

Figure 5. A. Exposure in the El Carrizal site showing a steep fault dip of ~60° for the Pan de Azúcar strand of the Las Chacras Fault Zone. B&C. Close-up view of clasts offset by similar steeply-dipping minor strands of the fault zone.

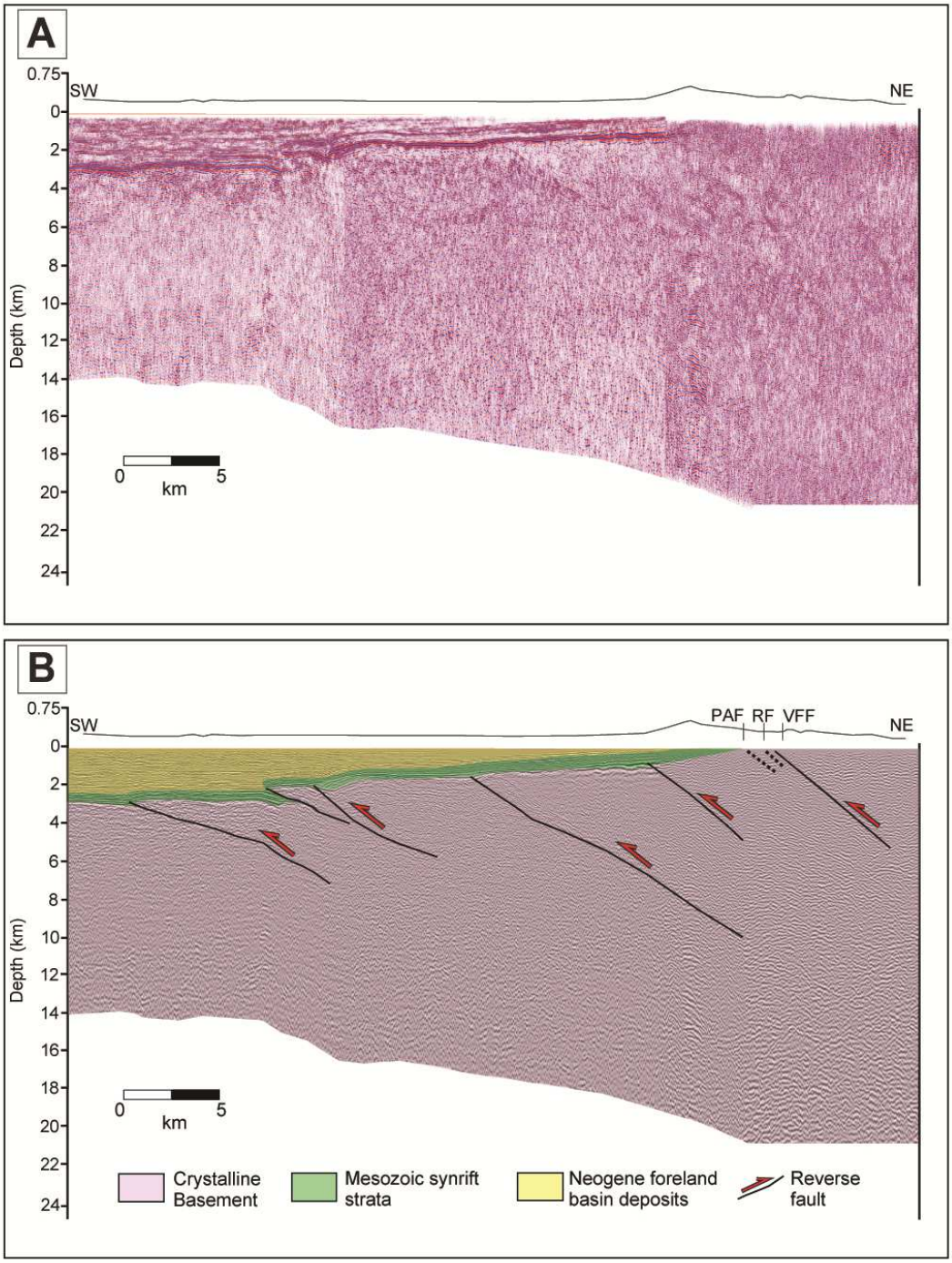

Figure 6. Seismic reflection line across the western Sierras Pampeanas structures in the southern extension of the Valle Fértil-La Huerta Range (see location of the profile in Fig. 2). A. without interpretation B. with interpretation showing the Valle Fértil Fault (VFF), unnamed faults west of the VFF and east of the Pie de Palo, and the projected traces of the Pan de Azúcar (PAF) and Rickard Fault (RF) strands of the LCFZ. Topography has a 5x vertical exaggeration.

4. Site analysis

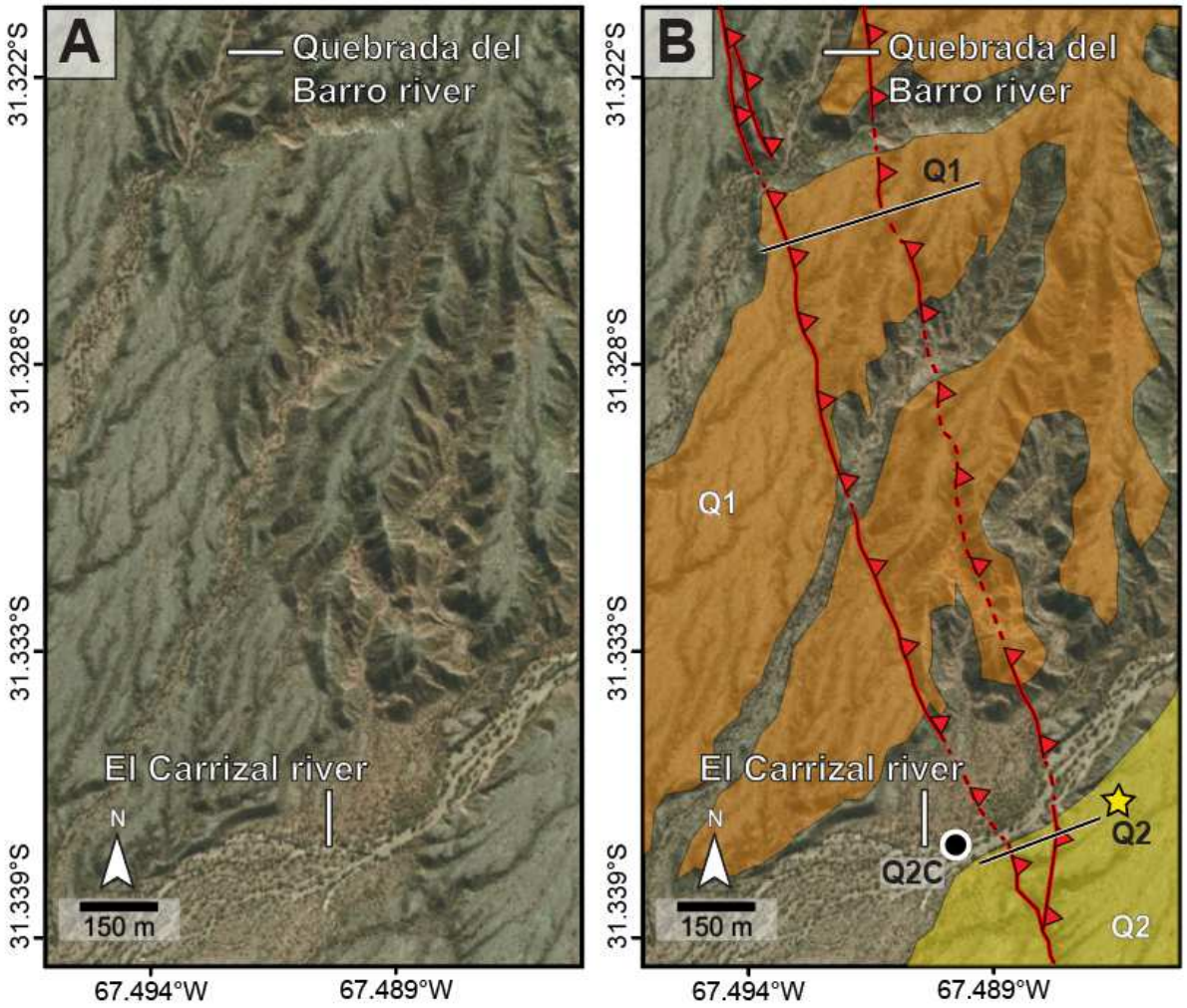

Figure 7. Detailed view of faulted alluvial fan surfaces at the Quebrada del Barro, and El Carrizal sites (see location in Fig. 3) superimposed on a Bing Maps aerial image (Copyright Bing Maps). A. without interpretation B. with interpretation. The black lines in indicate the location of topographic profile survey lines shown in Fig. 10; stars indicate ^{10}Be surface sample locations; and the black circles indicate the location of active channel sample locations.

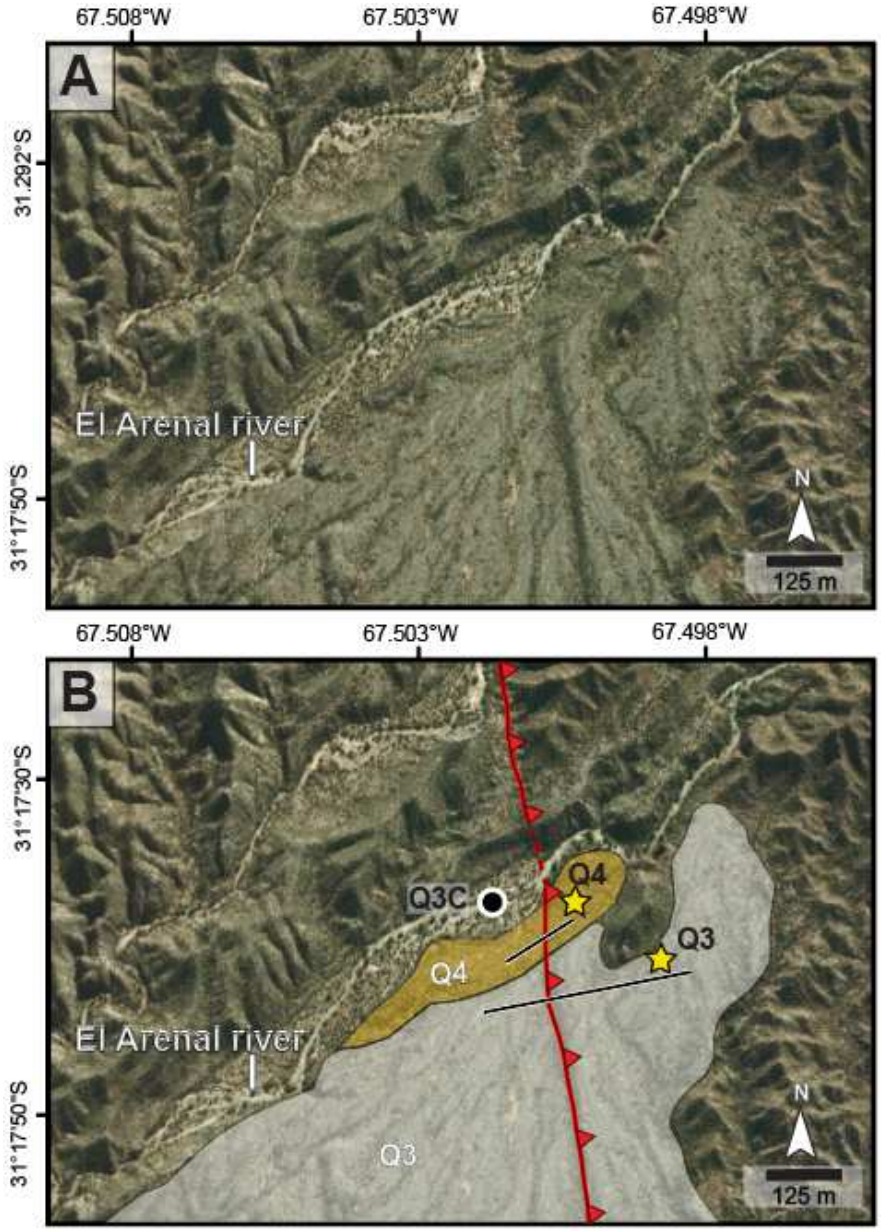

Figure 8. Close-up view of faulted alluvial fan surfaces at the El Arenal site (see location in Fig. 3) superimposed on a Bing Maps Aerial image (Copyright Bing Maps). A. without interpretation B. with interpretation. The straight black lines indicate the location of topographic profile survey lines; stars indicate ^{10}Be surface sample locations; and the black circles indicate the location of active channel sample locations.

4.1. Quebrada del Barro, El Carrizal, and El Arenal Sites

The west-facing, downslope-directed scarps of the Pan de Azúcar strand of the LCFZ exhibit their greatest displacement in the vicinity of the Quebrada del Barro and El Carrizal rivers (**Figs. 3, 4, 7, & 10**), with cumulative scarps reaching up to ~20-m-high. The fault, which trends N15°W, bifurcates towards the north around 200 m south of the El Carrizal river, with the western trace being more continuous than the eastern trace. These scarps displace relatively well preserved late Quaternary alluvial fans. Profile views of the large cumulative scarps of the LCFZ can be seen

along both the Quebrada del Barro and El Carrizal rivers. (**Figs. 3 & 4**). These scarps uplift and expose the westward younging, gently west-dipping Triassic syn-rift sequences involving the Quebrada del Barro, Carrizal, and Esquina Colorada Formations, which suggests reactivation of extensional Triassic rift structures. Whether or not the Las Chacras fault's continuation in the subsurface connects with the range front-bounding Valle Fértil Fault, and therefore represents a footwall shortcut, remains uncertain. Farther north in the El Arenal site, the LCFZ exhibits much smaller scarps that reach elevations only as high as ~5 m and displace both alluvial fans and strath terraces ('Q3' and 'Q4' in **Fig. 8**).

An exposure in the El Carrizal site shows a steep fault dip of ~60° (**Fig. 5**) which is consistent with the steep dips measured in most other faults in the Sierras Pampeanas region. Some faults in the eastern Sierras Pampeanas reach nearly vertical orientations, due to their origin as reactivated listric normal faults related to earlier rifting events (e.g., Guerrero et al., 1993; Ragona et al., 1995; Furque et al., 1998; Vujovich et al., 1998; Bonalumi et al., 1999; Caselli et al., 1999; Ramos & Vujovich, 2000; Candiani et al., 2001; Ramos et al., 2002; Richardson et al., 2013; Siame et al., 2015; Bellahsen et al., 2016).

4.1.1. Alluvial Fan Surfaces

We focus on the Quebrada del Barro, El Carrizal, and El Arenal sites because they preserve prominent (up to ~20-m-high) cumulative-displacement scarps of the LCFZ, cutting through an areally extensive and well-preserved suite of successively younger alluvial fans/strath terraces (Q1, Q2, Q3, and Q4; **Figs. 4, 7 & 8**).

The alluvial surfaces have an average slope of 2–3° to the west and 3–4° to the south and form an angular unconformity with the Triassic Quebrada del Barro, Carrizal, and Esquina Colorada Formations. The covering material of the surfaces is composed mostly of pebble- to cobble-sized clasts of varied lithologies including quartzite, quartz tonalite, quartz diorite, amphibolite, mica-garnet-feldspar gneiss and schist have been transported by southwest-directed channels from the Proterozoic Valle Fértil complex on the western flank of the Sierra de Valle Fértil-La Huerta range.

Relief of the upthrown portion of alluvial surfaces Q1, Q2, Q3, and Q4 relative to their corresponding adjacent streams are on average 25, 20, 17, and 14 m, respectively. The relative age of the surfaces is based on relief but is also consistent with textural characteristics observed on each surface. In terms of grain size, Q1 and Q2 are relatively well-sorted, while Q3 and Q4 are moderately- and poorly-sorted, respectively. In terms of roundness, Q1 has angular to sub-angular grains, Q2 and Q3 both have sub-angular to sub-rounded grains, and Q4 has sub-rounded to rounded grains. Clasts on the older surfaces tend to be smaller, well-sorted, and have sharp edges due longer periods of mechanical weathering of originally larger clasts. All surfaces exhibit desert varnish, but more noticeably so on the older surfaces Q1 and Q2. Pedogenic development was observed to be more advanced in older surfaces. In addition, all surfaces exhibit a clast-supported framework and

development of desert pavement, characteristic of surfaces formed in semi-arid climates.

4.1.2. Ages

Table 1. The ^{10}Be Sample Data -Las Chacras Fault Zone

Sample no.	Sample type[a]	Latitude (°S)	Longitude (°W)	Elevation (m)	Material[b]	Thickness (cm)	Topographic shielding	Quartz mass (g)	Be carrier mass (g)	Be carrier concentration (mg/g)[c]	^{10}Be/^{9}Be (10^{-15})[d]	10 Be concentration (10^{5} atom Be/g Qtz)	Exposure age and uncertainties (ka) [e, f, g, h]	KDE Exposure age (ka)[i]
Surface samples														
Q2	A	31.3365	67.48653	791	Q, T, D, A, G/S	4	0.99993	14.882	0.3478	1045.9	182.55 ± 7.97	2.96 ± 0.13	40.5 ± 3.6 (1.8)	—
Q2SA	C	31.33645	67.48678	791	Q	4	0.99993	14.484	0.3453	1045.9	128. 96 ± 4.61	2.13 ± 0.08	29.4 ± 2.5 (1.1)	28.1 ± 4.5
Q2SB	C	31.33647	67.48680	791	Q	4	0.99993	16.965	0.3055	1045.9	129.48 ± 4.84	1.61 ± 0.06	22.7 ± 1.9 (0.9)	28.1 ± 4.5
Q2SC	C	31.33646	67.48677	791	Q	4	0.99993	7.5479	0.3005	1045.9	93.90 ± 3.43	2.57 ± 0.10	35.6 ± 3.0 (1.4)	28.1 ± 4.5
Q2SD	C	31.33648	67.48673	791	Q	4	0.99993	11.159	0.2993	1045.9	107.59 ± 4.16	1.99 ± 0.08	27.5 ± 2.4 (1.1)	28.1 ± 4.5
Q3	A	31.2948	67.49817	920	Q, T, D, A, G/S	4	0.99824	20.315	0.3239	984.8	152.45 ± 7.28	1.79 ± 0.09	23.0 ± 2.1 (1.1)	—
Q4	A	31.29340	67.49967	914	Q, T, D, A, G/S	4	0.99824	17.508	0.3001	1045.9	82.35 ± 3.25	0.97 ± 0.04	13.4 ± 1.2 (0.6)	—
Channel Samples														
Q2C	A	31.33697	67.48883	764	Q, T, D, A, G/S	4	0.99869	22.09	0.3239	984.8	38.41 ± 3.53	0.38 ± 0.04	6.3 ± 0.8 (0.6)	—
Q3C	A	31.29282	67.49993	898	Q, T, D, A, G/S	4	0.99824	8.2476	0.3075	1045.9	13.79 ± 1.16	0.32 ± 0.03	5.0 ± 0.6 (0.5)	—

— Indicates no data or not applicable.

[a] A= amalgamation; C= individual clast.

[b] A= Amphibolite; D= Quartz Diorite; G/S= Mica-Garnet-Feldspar Gneiss/Schist; Q= Quartzite; T = Quartz Tonalite.

[c] Q3 and Q2C were analyzed using another bottle of ^{9}Be carrier also provided by Abaz Alimanovic of the University of Melbourne. Inevitably, each 9Be carrier bottle generally has a slightly different concentration.

[d] 07KNSTD is the standard used by PrimeLab for their AMS measurements.

[e] Ages were computed using "Lm" scaling scheme.

[f] Ages were computed assuming zero erosion and zero inheritance.

[g] Uncertainties presented are external or total uncertainties and internal uncertainties (in brackets).

[h] The current version (v3) of the online calculator by Balco et al. (2008) uses a sea level and high latitude (SLHL) production rate value of 4.01 ± 0.33 atoms/g SiO_2 from the calibration dataset in Borchers et al. (2016).

[i] KDE age pertain to the average of all the individual clasts' ages

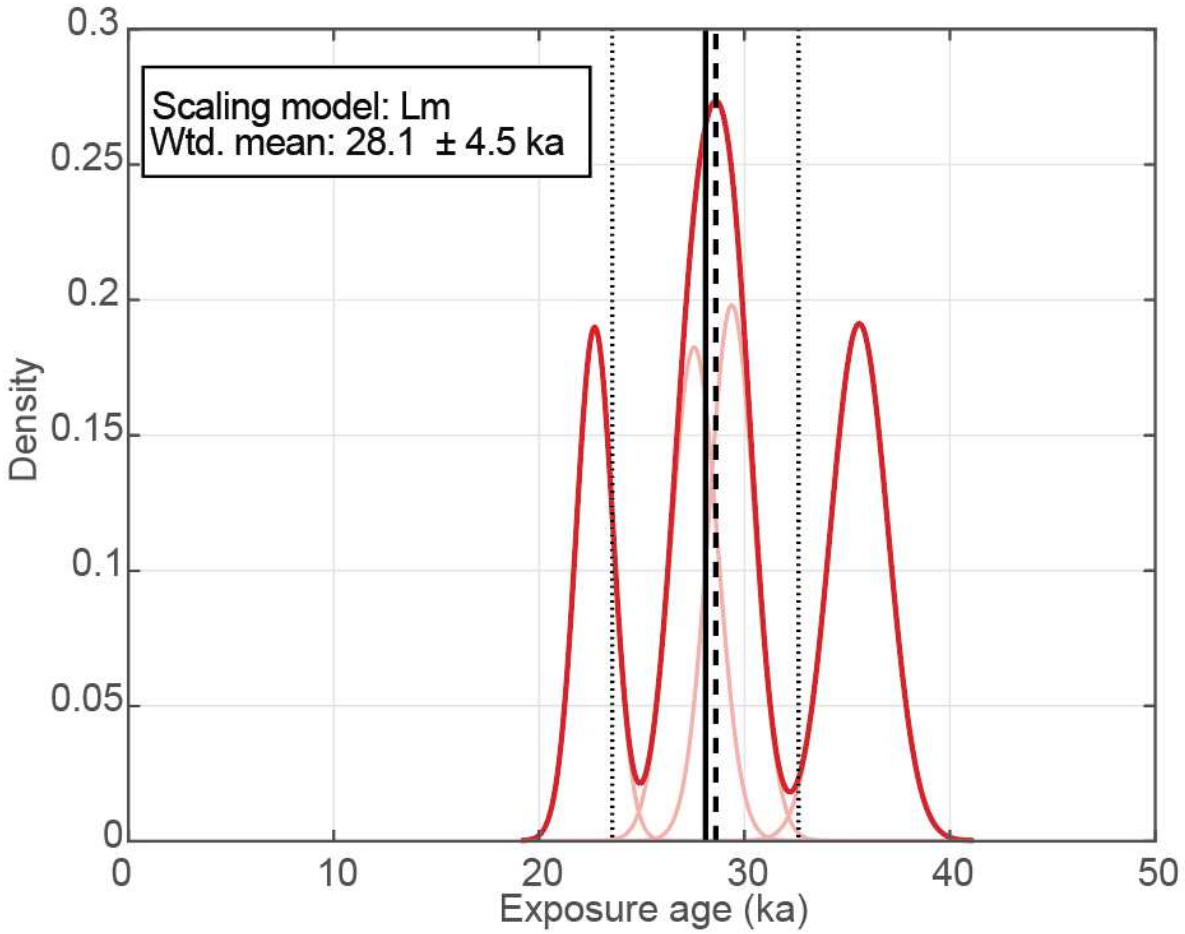

Figure 9. Kernel density estimation (KDE) of Q2 clast ages (Q2SA, Q2SB, Q2SC, and Q2SD in Table 1). Light red lines represent the probability distribution of each individual clast, bold red line indicates the summed distribution of the dataset, solid black line indicates the weighted mean, black dashed line indicates the mode, and dotted black lines indicate the weighted standard deviation. Refer to figure 7 for Q2 sample location.

Samples were collected from the hanging wall side of each fault-displaced alluvial surface. We were unable to obtain an age for surface Q1 (**Fig. 7**) due to insufficient quartz extracted from most of the depth profile samples. ^{10}Be ages for Q2 (**Fig. 7**) were computed both from amalgamated surface clast samples and a subset of four individual surface clasts (Q2SA, Q2SB, Q2SC, Q2SD in **Table 1**).

The amalgamated clasts surface exposure ages (**Table 1**) represent average ages of alluvial surfaces, with an uncertainty that is related to the analytical measurement and, implicitly, the actual spread of the ages of individual clasts (Anderson et al., 1996; Repka et al., 1997). Scatter in ages of individual clasts from the same alluvial surface could be caused by dissimilar inheritance related to diverse pre-depositional exposure histories of clasts, protracted alluvial surface abandonment, and post-depositional mixing and/or erosion (e.g., Repka et al., 1997; Gosse and Phillips, 2001; Dühnforth et al., 2012). In order to explore the reliability of our amalgamated samples, we extracted four clasts from the Q2 sample for individual analysis. We examine these clast ages using a kernel density estimate (KDE) plot. These sample ages, which were calculated assuming zero erosion and

zero inheritance, range from 22.7 ± 1.9 to 35.6 ± 3.0 ka (**Fig. 9**), yielding a KDE weighted average age of 28.1 ± 4.5 ka. This average age is younger than the Q2 amalgamation age that was calculated with the same inheritance and erosion assumptions (Table 1), as well as the inheritance-corrected Q2 amalgamation age (by ~7 ka, see Table 2). Older ages from cobbles or boulders in such alluvial fan surfaces are typically interpreted to reflect higher inheritance due to prolonged exposure on hillslopes or earlier episodes of deposition (Owen et al., 2011; Frankel et al., 2007). Younger ages are often used to approximate the age of surface abandonment (Brown et al., 1998; Riihimaki et al., 2006; Matmon et al., 2009). However, while we took care in collecting thin flat samples with visible desert varnish (an indication of surface stability), we cannot entirely rule out post-depositional erosion and/or exhumation (Frankel et al., 2007). Further complicating our interpretation, a recent modeling study found that surface abandonment can take place long after the deposition of the youngest clast (D'Arcy et al., 2019).

An amalgamation age, which has a larger clast population of 30, statistically averages out possible preexposure nuclide concentration outliers or post-depositional erosion or exhumation and, therefore, must provide a more reliable estimate of the average age of the surface (Anderson et al., 1996; Repka et al., 1997). Further, previous studies at similar latitudes in the Precordillera of Argentina show that cosmogenic surface ages from inheritance-corrected amalgamated clast samples are comparable to ages from depth profiles (Schmidt et al., 2019; Rimando et al., 2019), and consistent with independent ages from ^{14}C dating (e.g., Schmidt et al., 2011a).

However, as with depth profiling, the quality of the amalgamation age is dependent on how well inheritance and erosion rates can be constrained at each site. Due to the lack of reliable independent surface age determinations (e.g., Blisniuk et al., 2012; Le Dortz et al., 2012) and independent inheritance and erosion rate constraints, it is currently not possible to assess how much our amalgamated clast surface ages might deviate from the "actual" surface age. Using the non-zero ^{10}Be concentrations of clasts from the modern channel for inheritance correction of alluvial surface clasts is a case in point. Doing so assumes that the modern channel exhibits conditions identical to those under which the alluvial surface was formed in the past. In other words, the assumed 'inheritance' values are only meaningful if long-term erosion rates at the source area and channel transport rates remained the same. Using this 'inheritance' would be invalid, for instance if the present-day erosion rates are very slow or close to zero; the ~5-6 ka 'inheritance' measured in the modern channel, could then possibly be just a result of a single major erosional event that initiated incision at ~5-6 ka. Another possibility is that modern channel ^{10}Be concentrations could be composed of reworked clasts derived from 'cannibalization' of sediments from older alluvial deposits (Siame et al., 2015; Foster et al., 2017). Improperly constrained modern channel 'inheritance' values, arising from the aforementioned illustrated situations could therefore have the effect of

either overestimating or underestimating 'inheritance'-corrected alluvial surface exposure ages. Furthermore, the age scatter and the lower average KDE age of Q2 (Table 1, Figure 9), indicates that the surface may have had a complex evolution. Some of the possible explanations for such an age scatter are: 1) that the chosen four individual clasts are outliers that bear significantly lower inheritance relative to other clasts in the amalgamation (or no inheritance at all), 2) that these clasts may have had different erosion histories from the rest of the clasts in the amalgamation, or 3) a more complicated combination of these two situations.

Table 2. ^{10}Be Surface Age Scenarios

Sample no.	Sample type[a]	Ages (ka)[b,c,d]					
		inheritance	no inheritance correction (zero inheritance)				
		no erosion	w/ erosion				
		0 mm/ka	1 mm/ka	2 mm/ka	3 mm/ka	4 mm/ka	5 mm/ka
Q2	A	35.8 ± 3.3 (1.9)	41.7 ± 3.8 (2.0)	43.2 ± 4.1 (2.1)	44.9 ± 4.5 (2.3)	47.3 ± 4.9 (2.5)	50.2 ± 5.5 (2.8)
Q2SA	C	24.5 ± 2.2 (1.2)	30.1 ± 2.6 (1.2)	30.9 ± 2.8 (1.2)	31.9 ± 2.9 (1.3)	32.9 ± 3.1 (1.4)	34.1 ± 3.3 (1.5)
Q2SB	C	17.9 ± 1.7 (1.1)	23.1 ± 2.0 (0.9)	23.5 ± 2.1 (1.0)	24.0 ± 2.2 (1.0)	24.5 ± 2.3 (1.1)	25.0 ± 2.4 (1.1)
Q2SC	C	30.1 ± 2.7 (1.5)	36.7 ± 3.2 (1.5)	37.8 ± 3.4 (1.6)	39.0 ± 3.7 (1.7)	40.3 ± 3.9 (1.8)	41.5 ± 4.2 (2.0)
Q2SD	C	22.7 ± 2.1 (1.3)	28.2 ± 2.5 (1.2)	28.8 ± 2.6 (1.2)	29.6 ± 2.7 (1.3)	30.3 ± 2.9 (1.4)	31.2 ± 3.1 (1.5)
Q3	A	19.3 ± 1.9 (1.3)	23.4 ± 2.2 (1.2)	23.8 ± 2.2 (1.2)	24.3 ± 2.3 (1.3)	24.8 ± 2.4 (1.3)	25.3 ± 2.6 (1.4)
Q4	A	9.4 ± 1.0 (0.8)	13.5 ± 1.2 (0.6)	13.6 ± 1.2 (0.6)	13.8 ± 1.2 (0.6)	13.9 ± 1.3 (0.6)	14.0 ± 1.3 (0.6)

[a]A= amalgamation; C= individual clast.

[b]Inheritance correction was done by subtracting the concentration of adjacent channel samples in Table 1 (e.g., Q2C from Q2 and Q3C from Q3 and Q4) before computing ages.

[c]Ages were computed using "Lm" scaling scheme.

[d]Uncertainties presented are external or total uncertainties and internal uncertainties (in brackets).

Because we cannot definitively estimate inheritance and erosion rates that could explain the age scatter in Q2 and the non-zero ^{10}Be concentration in the modern channel clasts, there is a need to take all these possibilities into consideration in calculating ages. We therefore calculate a range of amalgamated ages, and consequently slip rates, for each surface in this study based on a range of possible inheritance and erosion rates. We thus define two end-member scenarios of inheritance and erosion rates for calculating our amalgamation ages: zero erosion and significant inheritance (scenario 1) and; significant erosion and zero inheritance (scenario 2). Amalgamated ages that assume zero erosion and zero inheritance are presented in Table 1, while the end-member amalgamated ages are presented in Table 2.

Assuming zero erosion could be justified by the observed ubiquity of desert varnish, which is an indication of high degree of surface preservation (e.g., Jakica et al., 2011; Rimando et al., 2019). Further, zero erosion has also been assumed in other slip rate studies employing cosmogenic dating in several sites along the Precordillera and the Sierras Pampeanas (Costa et al., 2019; Hedrick et al., 2013; Rimando et al., 2019; Schmidt et al., 2011a; Siame et al., 2002). Alluvial surfaces are more likely than not to have a component of inherited nuclide concentration (e.g., Lal, 1991; Anderson, et al., 1996; Repka et al., 1996; Blisniuk et al., 2012; Brocard et al., 2003). We therefore estimated surface ages for Q2, Q3, and Q4 (**Fig. 7 & 8**)

using amalgamated clasts, correcting inheritance by subtracting the ^{10}Be concentration of the adjacent active channel samples. As noted earlier in section 3.2, the estimated inheritance values from the ^{10}Be concentration of the active channel samples are only valid if the long-term erosion rates have not varied significantly. Assuming the conditions of the zero erosion-significant inheritance scenario are true, Q2 yields an age of 35.8 ± 3.3 ka, Q3 yields an age of 19.4 ± 1.9 ka, and Q4 yields an age of 9.4 ± 1.1 ka (**Table 2**). The difference between the ages yielded by the amalgamated samples and the average KDE age for Q2 in scenario 1 could then be explained by either: 1) the presence of much younger clast ages in Q2 due to renewed aggradation since the onset of the last glacial maximum (LGM), or 2) the amalgamation having an unusually large number of high-inheritance clasts that cannot be accounted for even by subtracting the ^{10}Be concentration from the active channel clasts.

Conversely, assuming significant erosion rates and zero inheritance could also explain the large scatter in ages and lower average age shown by the KDE (Figure 9). If significant erosion occurred, then it is possible to hypothesize a significant underestimation of at least some of the individual clast ages that were previously calculated by assuming zero erosion (**Table 2, Figure 9**). We calculated ages using a maximum erosion rate of 5 mm/ka. This is based on a reasonable range of erosion rates for semi-arid regions (Portenga & Bierman, 2011) of ~1–5 mm/ka, which were constrained through depth profile modelling in the nearby easternmost Precordillera (Hedrick et al., 2013; Rimando et al., 2019, and references therein). Under the conditions of scenario 2, Q2 yields an age of 50.2 ± 5.5 ka, Q3 yields an age of 25.3 ± 2.6 ka, and Q4 yields an age of 14.0 ± 1.3 ka (**Table 2**). We then explored the effects of assuming zero erosion on the zero-inheritance amalgamation ages by determining the percent error compared to ages recalculated using minimum and maximum erosion rates of 1 and 5 mm/ka, respectively. Our results indicate that using 1 mm/ka of erosion yields ages for Q4, Q3, and Q2 surfaces that are underestimated by 1, 2 and 3% of the zero-erosion, zero-inheritance ages, respectively. Recalculating ages using 5 mm/ka erosion rate has a stronger effect: ages for Q4, Q3, and Q2 surfaces are underestimated by 4, 10, and 24% of the zero-erosion ages, respectively. The ^{10}Be amalgamation ages should therefore be considered minimum ages. However, especially for larger clasts, cosmogenic ages are likely to be overestimated due to the inability to fully account for inheritance rather than underestimated due to erosion.

The ^{10}Be ages of Q2, Q3, and Q4 calculated using both scenario 1 and 2 are consistent with the surfaces' relative ages determined by relief, textural features, and pedogenic development, suggesting that surface clast amalgamation ages are reliable in the El Carrizal and El Arenal sites (**Figs. 3, 7 & 8**). Along with the analytical and geological uncertainties associated with the samples we dated, surface exposure ages may also be affected by assumptions that were made in the age calculation (Balco et al., 2008). In particular, the same nuclide concentrations indicated in Table 1 may yield different exposure ages under a different set of assumptions (e.g., production rates and scaling schemes). All the ^{10}Be data used in calculating ages is listed in Table 1 to allow recalculation of exposure ages with

future improvements in dating techniques. We note that the 'Lm' scaling scheme (Nishiizumi et al., 1989; Lal, 1991; Stone, 2000) yields ages that are consistently lower than ages calculated using the Lifton-Sato-Dunai or 'LSDn' scaling scheme (Lifton et al., 2014) and slightly higher/lower than ages calculated using the 'St' scaling scheme (Lal, 1991; Stone, 2000) (**see supplementary figures S7-S13**).

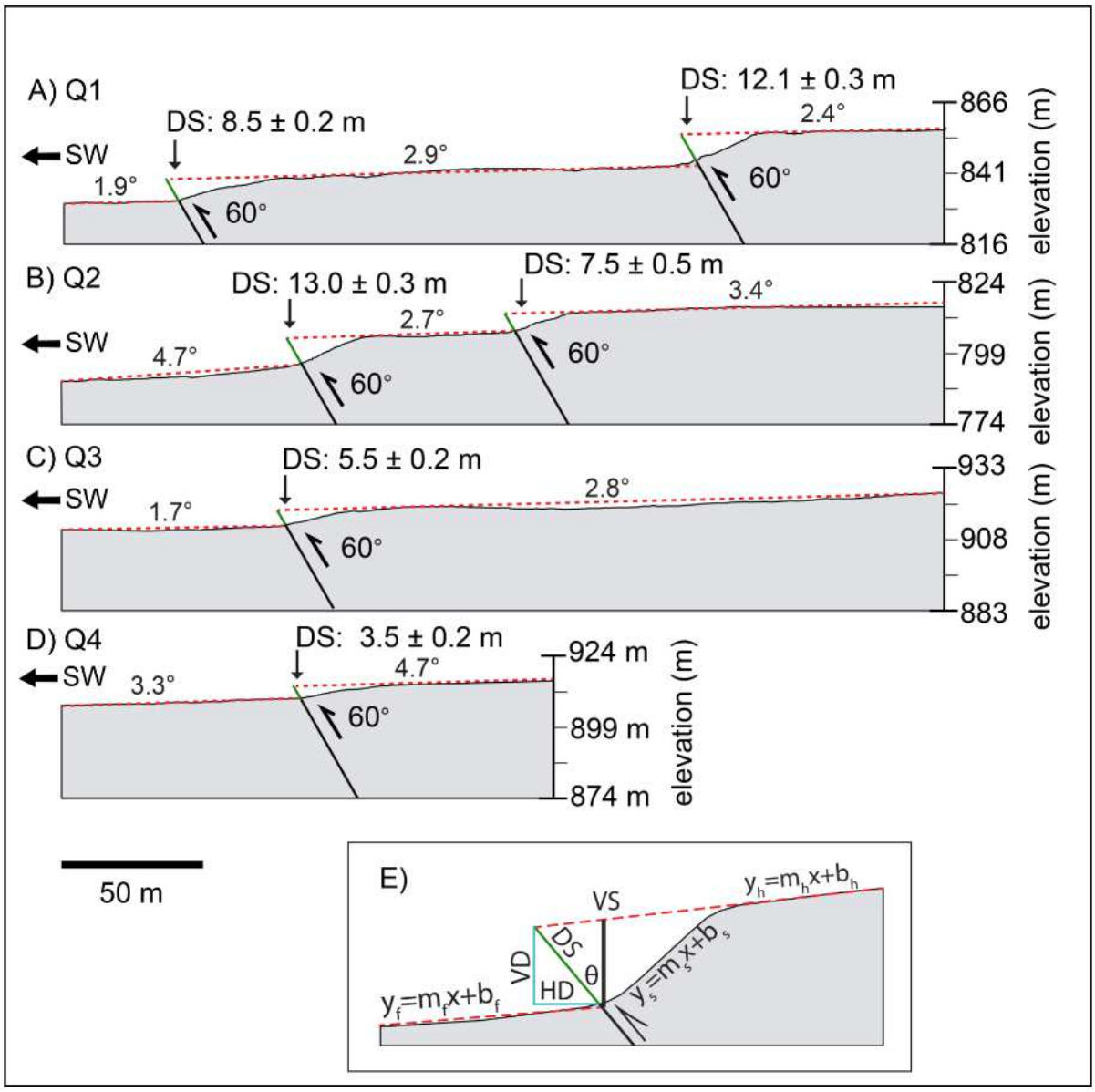

Figure 10. DGPS scarp topographic profiles used to calculate displacement of the Las Chacras Fault. Slopes of the upthrown, downthrown, and scarp surfaces and a field observed fault dip of 60°E are used to compute the displacement as described in Yang et al. (2015). See Figures 7 and 8 for profile locations. In figure 10E, VD – vertical displacement, HD – horizontal displacement, VS – vertical separation, DS- dip-slip displacement; f, s, and h subscripts in the linear equations correspond to footwall, scarp, and hanging wall, respectively. Dashed red line represents the hanging wall and footwall surface linear fits, blue lines correspond to VD and HD, and green line corresponds to DS.

4.1.3. Displacement

We used scarp topographic profiles measured though DGPS survey of a suite of three successively younger alluvial fans (Q1, Q2, Q3) and one strath terrace (Q4) from the Quebrada del Barro, El Carrizal and El Arenal sites as markers to compute displacement (dip-slip, shortening, and uplift) according to the methodology described in Yang et al. (2015). Our results are presented in Figure 10.

Our results show that there is a relationship between the age of the surface and the amount of displacement measured (**Table 3**). The measured displacement is highest on Q1 but is very similar to displacement measured on Q2. Although we were unable to calculate surface exposure ages for Q1, the OSL age determined by Rothis et al. (2019) of 47.8 ± 8.3 ka suggests that there may be only a small difference in age between Q1 and Q2. The similarity in displacement of Q1 and Q2 could be explained by along-strike variation in displacement on the fault either consistently or in a single past earthquake. This could be achieved through lower slip along the portion of the fault that cuts Q1 at the Quebrada del Barro site or higher slip along the portion of the fault that cuts Q2 at the El Carrizal site (Figs. 3&7). Alternatively, the period between the formation of Q1 and Q2 may have been characterized by tectonic quiescence.

The displacement measured on Q3 of 5.5 m (**Table 3**) is much lower compared to that measured on Q2 of 20.5 m; this is expected considering the ~15 ka age difference between these two surfaces. The minimal difference in the displacement (uplift, shortening, or dip-slip) measured on Q3 and Q4 of ~0.1 m (**Table 3**) is consistent with the narrower age difference of these two surfaces.

While some ephemeral channels that cross the LCFZ appear to be displaced left-laterally (which is the expected kinematics of the fault given its strike), constraining a strike-slip component to displacement proves quantitatively challenging due to the absence of preserved, well-defined piercing points (i.e., multiple, successive terrace risers and treads) that will allow distinguishing the amounts of separation (a.k.a. apparent slip) from actual lateral-slip on these streams that cut across the fault scarp diagonally.

Table 3. Dip-slip displacement, shortening, and uplift calculated from the scarps of the Las Chacras Fault Zone[a]

Surface	Total displacement		
	Dip-slip (m)	Shortening (m)	Uplift (m)
Q1	20.6 ± 0.4	10.3 ± 0.2	17.9 ± 0.3
Q2	20.5 ± 0.6	10.2 ± 0.3	17.8 ± 0.5
Q3	5.5 ± 0.2	2.7 ± 0.1	4.7 ± 0.2
Q4	3.5 ± 0.2	1.7 ± 0.1	3.0 ± 0.2

[a]displacement was calculated assuming a dip of 60° ± 5°.

4.1.4. Slip rates

We calculated the slip rate (**Table 4**) of each cumulatively displaced alluvial fan/strath terrace by dividing the total offset of the surface by its exposure age. It should be noted that the slip rates we calculate here are based on measurements taken from only a few sites, thereby presenting additional uncertainty (related to site selection) in the estimation of slip rates for the entire Pan de Azúcar strand of the LCFZ.

On surface Q2, dip-slip, shortening, and uplift rates measured are ~0.4–0.6, ~0.2–0.3, and ~0.3–0.5 mm/yr, respectively; on surface Q3, ~0.2-0.3, ~0.1, and ~0.2 mm/yr; and on surface Q4, ~0.3–0.4, ~0.2, and ~0.3 mm/yr. Average dip-slip, shortening, and uplift rates measured on surfaces Q2, Q3, and Q4 are ~0.3-0.4, ~0.2, and ~0.3–0.4 mm/yr, respectively. Our data show that at least since ~36-50 ka, slip rates have varied slightly along the Pan de Azúcar strand of the LCFZ (**Table 4**). Slip rates measured from Q2 are the highest and decrease to almost half for Q3 and increase slightly for Q4. It should be noted that since alluvial surface exposure ages constrain the period of active deposition of sediments (which may span significant durations), rather than abandonment (e.g., Owen et al., 2011; D'Arcy et al., 2019), ages may be overestimated due to inheritance. Additionally, if there have been variable erosion rates related to local, short-term extreme events in the sediment source area, inheritance values estimated from active channel clasts may be underestimated. For areas characterized by low erosion rates (~1 mm/ka), the uncertainty introduced to inheritance estimates is expected to be less than 10% (e.g., Bierman & Steig, 1996; González et al., 2006). For these reasons, these slip rates should be considered a minimum.

Slip rates of the Rickard strand of the LCFZ (**Fig. 3**) are much lower than those measured along the Pan de Azúcar strand. Scarps along the Rickard strand are only ~2 m high (Rothis et al., 2019); they displace the ~36–50 ka Q2 surface, yielding shortening and uplift rates of only ~0.02–0.03 and ~0.04–0.05 mm/yr, respectively. We were unable to measure slip rates on Rickard strand of the LCFZ due to the lack of well-preserved, displaced geomorphic features.

Table 4. Dip-slip, shortening, and uplift rates calculated from the cumulative scarps of the Las Chacras Fault Zone

	Scenario 1 slip rates[a]			Scenario 2 slip rates[b]		
Time interval	Dip-slip rate (mm/yr)	Shortening rate (mm/yr)	Uplift rate (mm/yr)	Dip-slip rate (mm/yr)	Shortening rate (mm/yr)	Uplift rate (mm/yr)
Q2-present	0.6 ± 0.1	0.3 ± 0.0	0.5 ± 0.1	0.4 ± 0.0	0.2 ± 0.0	0.3 ± 0.1
Q3-present	0.3 ± 0.0	0.1 ± 0.0	0.2 ± 0.0	0.2 ± 0.0	0.1 ± 0.0	0.2 ± 0.0
Q4-present	0.4 ± 0.1	0.2 ± 0.0	0.3 ± 0.0	0.3 ± 0.0	0.2 ± 0.0	0.3 ± 0.0
Average	0.4 ± 0.0	0.2 ± 0.0	0.4 ± 0.0	0.3 ± 0.0	0.2 ± 0.0	0.3 ± 0.0

[a]Scenario 1 slip rates are based on ages that assumed a 0 mm/ka erosion rate and that were corrected for inheritance

[b]Scenario 2 slip rates are based on ages that assumed a 5 mm/ka erosion rate and that were not corrected for inheritance

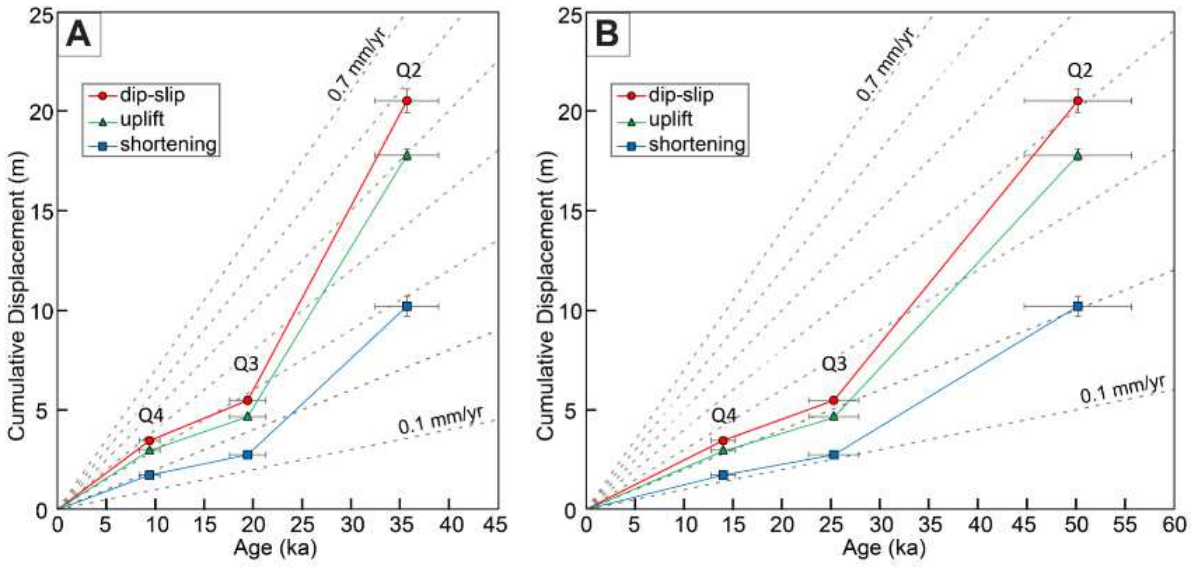

Figure 11. Dip-slip, uplift, and shortening components of cumulative displacement (and their uncertainties) along the Pan de Azúcar strand against age for surfaces Q2, Q3, and Q4. Dashed lines, which were constructed by dividing displacement by age, indicate theoretical uniform slip rates which can be used as visual reference for graphically determining slip rates. A) Plot for slip rates calculated using ages which assume scenario 1 inheritance and erosion rates. B) Plot for slip rates calculated using ages which assume scenario 2 inheritance and erosion rates.

5. Discussion

5.1. Late Quaternary activity of the Las Chacras Fault Zone

We determine average and maximum shortening of ~0.2 mm/yr and ~0.3 mm/yr, respectively, along the Pan de Azúcar strand of the LCFZ. Rothis et al. (2019) estimated a shortening rate of 0.16 ± 0.1 mm/yr along the same structure that agrees with our measurements. However, their methods are problematic. To calculate slip rate, they used a fault dip of 25°E, which is inconsistent with our field observations and regional fault data, which support a dip of ~60°E. Further, they used the vertical separation and age difference of OSL samples from hanging wall exposures immediately adjacent to the fault plane, to determine slip rate. We note that age trends in these samples most likely reflect burial/deposition rather than an uplift rate. Rothis et al. (2019) suggest that the last movement on the fault occurred before ~12 ka. Our ^{10}Be age estimates indicate that the most recent movement along the LCFZ, based on the age of the youngest surface displaced by the Pan de Azúcar strand (Q4; **Table 1**), is ~9 ka (**Fig. 8**). This is generally consistent with Rothis et al.'s (2019) estimate considering the uncertainty in the assumed erosion rates for exposure age calculation. Alternatively, if there is a true discrepancy in the estimated timing of the fault's last movement, it is also possible that this could be a result of along-strike variability of slip on this fault during each earthquake.

Shortening rates measured along the LFCZ are relatively low compared to shortening rates along most Quaternary-active structures in the Precordillera region to the west, which reach up to 2 mm/yr (**Fig. 1**). The maximum shortening rate that we determine is similar to that of the Las Peñas Fault in the southern Precordillera (0.27 ± 0.11 mm/yr) in the last ~200 ka (Costa et al., 2019). However, this is an exceptionally low rate for the Precordillera, and is low even when compared to measurements on different time scales or other locations along the same fault (Schmidt et al., 2011a; Costa et al., 2019). The LCFZ's average and maximum uplift rates of ~0.3–0.4 and ~0.3–0.5 mm/yr, on the other hand, are comparable to uplift rates of structures in the Eastern Precordillera such as the La Laja and La Rinconada Fault (Rockwell et al., 2014; Rimando et al., 2019). This is likely due to the steep dip of the LCFZ (and most other faults in the Sierras Pampeanas) compared with most Precordilleran faults.

Because Quaternary slip rates have only been measured on two faults in the Sierras Pampeanas (Siame et al., 2015; this study), we cannot definitively determine how the cumulative shortening on structures in the Sierras Pampeanas compares to that of structures in the Precordillera. However, we can make several assumptions to explore strain distribution scenarios along a section through 31°S.

We estimate the total shortening rate across Pampean structures by using the few measured shortening rates as anchors (**Fig. 1A**). The shortening rate along the

westernmost measured fault in the Sierras Pampeanas, the Eastern Pie de Palo Fault (PdPE; see location on **Fig. 1B**) is ~ 0.3–0.5 mm/yr (assuming a 60° dip and the 0.5–0.8 mm/yr uplift rate determined by Siame et al., 2015). Although unmeasured, shortening rate on the Western Pie de Palo Fault may be similar (labelled as PdPW on **Fig. 1B**). While its sinuous mountain front, higher valley-floor-width to height ratios, and lower rates of seismicity suggest lower activity than along the eastern side of the range (**Fig. 1**), most other geomorphic indices used to characterize relative slip rates seem to be indistinguishable for both sides of the Pie de Palo (Rimando & Schoenbohm, 2020). The average shortening rate along the LCFZ (approximate location labelled as VF on **Fig. 1B**) is ~0.2 mm/yr since ~36–50 ka according to our study.

Both regional geomorphic studies (Rimando & Schoenbohm, 2020) and GPS studies (Brooks et al., 2003, and references therein) suggest that shortening rates decrease from west to east. GPS studies (Brooks et al., 2003, and references therein) provide the quantitative shortening rate estimates (4.5 ± 1.7 mm/yr across the Andean orogenic front). However, GPS observations are sparser (and exhibit decreasing precision) towards the east and can only be used to reliably infer strain distribution trends on decadal timescales. On the other hand, Rimando and Schoenbohm (2020) employ GIS-based measurement of geomorphic indices along fault-bound mountain ranges that span the entire Pampean flat-slab region from 30-32°S. This study presents average values of geomorphic indices for each fault such as hypsometric integral (HI), elongation ratio (Re), volume-to-area ratio (RVA), valley-floor-width-to-height (Vf) ratio, mountain front sinuosity (Smf), and the statistical moments of the hypsometric curve. While this approach is qualitative, it provides a longer-term assessment of regional slip rate trends (which could be applicable on Pleistocene timescales). Based on these arguments, if we assume that the shortening rate on faults to the east of the LCFZ is equal to or lower than the rate on the LCFZ itself, we can constrain the total shortening rate across the region. Our analysis suggests a minimum shortening rate of 0.8 mm/yr, assuming lowest rates on the Pie de Palo Faults and zero shortening on Pampean structures east of the LCFZ, across the Sierras Pampeanas at 31°S. Alternatively, by assuming maximum rates on the Pie de Palo faults and 0.2 mm/yr shortening each of the six Pampean faults east of the LCFZ, we can calculate a maximum shortening rate of 2.4 mm/yr (**Fig. 12**). If the ~0.7 mm/yr shortening rate of the Los Molinos Fault (located on Figure 1A) determined through line-restoration of a horizon in a paleoseismic trench is reliable (Costa et al., 2018), and there are also similarly high shortening rates east of the LCFZ, strain distribution pattern in the Sierras Pampeanas may be more complex. However, the higher slip rate measured along the El Molino Fault could be explained by distribution of shortening over fewer structures at 32.5°S latitude. A maximum total shortening on Pampean structures of ~2.4 mm/yr is equivalent to 30-40% of the total 5.5–7.7 mm/yr long-term geological (~20 Ma) shortening rate estimated for the entire cross section from the Principal Cordillera to the Precordillera from latitudes 30–33°S (Ramos et al., 2002, 2004; Zapata & Allmendinger, 1996), and ~50% of the 4.5 ± 1.7 mm/yr decadal slip rates determined by Brooks et al. (2003) across the Andean Orogenic Front (**Fig. 12**).

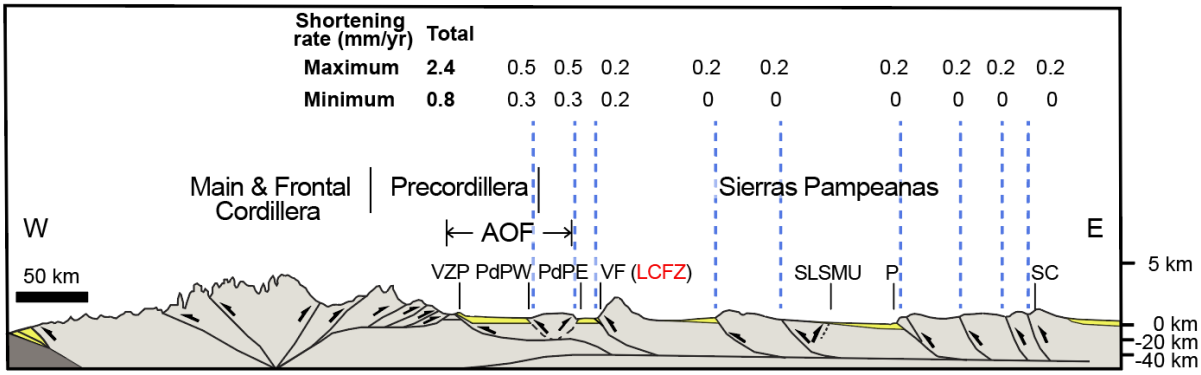

Figure 12. Schematic diagram showing possible maximum and minimum total shortening rates (mm/yr) for the Sierras Pampeanas from 30-31°S (see Fig. 1 for location). AOF—Andean orogenic front, VZP—Villicum-Zonda-Pedernal Fault, PdPW—Western Pie de Palo Fault, PdPE—Eastern Pie de Palo, VF—Valle Fértil Fault, , LCFZ—Las Chacras Fault Zone, SLSMU—Sierras de Los Llanos, Sierras de las Minas and Ulapes Fault, P—Pocho Fault, SC—Sierra Chica Fault Zone.

The decrease in shortening rate across the LCFZ and the abrupt decrease in geodetically inferred shortening rates at this longitude coincides with the resumption of normally dipping subduction of the Nazca plate between 67ºW and 68°W. Slab dip may exert control on this decrease in shortening rate, with lower shortening occurring on faults associated with a more normally dipping slab (30º to the east) due to a lower degree of plate coupling. However, in the case of the LCFZ, a lower shortening is also partly a result of having a steeper fault dip, which is characteristic of structures of the Sierras Pampeanas. To determine the control of slab dip on the level of activity of faults belonging to different tectonic styles (i.e., thin-skinned and thick-skinned), we refer to their dip-slip rates instead. The average dip-slip rate of the LCFZ of ~0.3–0.4 mm/yr is still lower than the ~1.1, ~0.5, and ~0.9–1.5 mm/yr dip-slip rates of the La Laja, La Rinconada, and Las Tapias faults, respectively, in the easternmost Precordillera. Therefore, similar to the findings of the relative tectonic activity assessment study by Rimando and Schoenbohm (2020), it appears that W-E shortening gradient shown by the decadal GPS velocity field reflects the longer-term gradient in slip rates of faults across the Pampean flat-slab segment.

5.2. Seismic Potential of the Las Chacras Fault Zone

To estimate the possible range of earthquake sizes the Pan de Azúcar strand of the LCFZ is capable of generating, it is first necessary to assess whether scarps correspond to single or multiple earthquake events. Displacement measured on alluvial fans Q2 and Q3 at the Quebrada del Barro, El Carrizal, and El Arenal sites, respectively, are too large to be single-event displacements in this tectonic setting (**Table 3**). The significant difference in their displacements (**Table 3**) also suggest that several events most likely took place between ~19 and 36 ka. Although the relatively small amount of discrete displacement on Q4 and Q3 (which is the

difference in cumulative displacement measured on Q3 and Q4) (**Table 3**), could have been generated in a single-event displacement, we are not able to provide independent constraints, such as from paleoseismic trenching, for the number and timing of past events. Since we cannot determine whether displacement on any of the scarps was a result of a single earthquake event, we cannot use displacement vs. earthquake magnitude scaling relationships (Wells & Coppersmith, 1994) to estimate seismic potential. Alternatively, assuming a scenario in which the entire length of the LCFZ ruptures, the surface rupture length vs. earthquake magnitude scaling relationships (Wells & Coppersmith, 1994) yields possible earthquake magnitude estimates ranging from M_W 6.5-7.1. However, Anderson et al. (1996, 2017) have shown that scaling relationships that include slip rates can provide better earthquake magnitude estimates.

Instead, we compute magnitude by calculating the arithmetic mean of slip rates measured from Q2 to Q4 and using the magnitude versus slip rate and fault length scaling relationships of Anderson et al. (1996, 2017). Using this approximation, the slip rate we measured, and a maximum surface rupture length of 30 km correlates with earthquake magnitude estimates ranging from M_W 6.7 to 7.1. These estimates are consistent with the magnitudes of earthquakes associated with Eastern Precordillera and Western Sierras Pampeanas faults in the region in 1944 (M_W 7.0), 1952 (M_W 6.8) and the 1977 (M_W 7.4). Although major cities in the province of San Juan may not be at risk for surface rupture of this fault, it should be noted that the sequence of the mainshock and aftershocks of the 1977 Caucete (San Juan, Argentina) earthquake, which was similarly distant from major cities, still caused strong ground-shaking, extensive liquefaction-related effects, and severe damage and triggering of shallow earthquakes on adjacent faults (INPRES, 1977, 1982, Alvarado et al., 2020).

6. Conclusions

We determined geomorphically-derived average shortening and uplift rates for the LCFZ for the past ~36-50 ka of ~0.2 and ~0.3–0.4mm/yr, respectively. Although slip rate has only been measured on a few faults in the Sierras Pampeanas region, the shortening rate we determine on the LCFZ is significantly lower than on most faults to its west both in the Precordillera and in the Sierra Pie de Palo of the western Sierras Pampeanas, revealing a general west-east decrease in shortening rates across the Pampean flat-slab. The LCFZ, with its abruptly lower shortening rate, also coincides spatially with the resumption of a more steeply-dipping Nazca plate between 67ºW and 68°W. Uplift rates, on the other hand, are relatively high and are comparable to those measured on faults in the Precordillera, likely resulting from the steeper dips of structures in the Sierras Pampeanas. From slip rate, fault length, and earthquake magnitude scaling relationships, the LCFZ is capable of generating earthquakes with magnitudes ranging from M_W 6.7 to 7.1. These potential earthquakes are large enough to pose considerable ground-shaking and

liquefaction-related hazards to nearby cities. Additional detailed analysis of event horizons from paleoseismic trenching are needed to provide further constraints on timing and recurrence of earthquakes associated with this fault.

7. Acknowledgments

This research was funded by a Natural Sciences and Engineering Research Council (NSERC) Discovery grant to Prof. Lindsay Schoenbohm. We acknowledge *Energía Provincial Sociedad del Estado* (EPSE), Government of San Juan, Argentina for providing us the seismic line data. We would also like to thank Petroleum Experts Limited for providing the MOVE™ academic license (https://www.petex.com/). The authors are grateful to Cesar Distante, Carolina Rivas (UNSJ, Argentina), and Gladis Balderramo (UNSJ, Argentina) for the field assistance.

8. Data Availability Statement

Data in this study were uploaded into the open-access Zenodo repository: Las Chacras Fault Zone, Argentina cosmogenic surface exposure ages. Retrieved from https://doi.org/10.5281/zenodo.4476736 (Rimando, 2020).

9. References

Allmendinger, R. W., Figueroa, D., Snyder, D., Beer, J., Mpodozis, C., & Isacks, B. L. (1990). Foreland shortening and crustal balancing in the Andes at 30ºS latitude. *Tectonics*, 9(4), 789-809. https://doi.org/10.1029/TC009i004p00789

Alvarado, P., Beck, S., Zandt, G., Araujo, M., & Triep, E. (2005). Crustal deformation in the south-central Andes backarc terranes as viewed from regional broad-band seismic waveform modelling. *Geophysical Journal International*, *163*(2), 580-598. https://doi.org/10.1111/j.1365-246X.2005.02759.x

Alvarado, P., & Beck, S. (2006). Source characterization of the San Juan (Argentina) crustal earthquakes of 15 January 1944 (M_W 7.0) and 11 June 1952 (M_W 6.8). *Earth and Planetary Science Letters*, 243(3), 615-631. https://doi.org/10.1016/j.epsl.2006.01.015

Alvarado, P., Beck, S., & Zandt, G. (2007). Crustal structure of the south-central Andes Cordillera and backarc region from regional waveform modelling. *Geophysical Journal International*, *170*(2), 858-875. https://doi.org/10.1111/j.1365-246X.2007.03452.x

Alvarado, P., M. Pardo, H. Gilbert, S. Miranda, M. Anderson, M. Saez, & S. Beck (2009), Flat-slab subduction and crustal models for the seismically active Sierras Pampeanas region of Argentina. *Backbone of the Americas: Shallow Subduction,*

Plateau Uplift, and Ridge and Terrane Collision, edited by S. M. Kay, V. Ramos and W. R. Dickinson, Geol. Soc. of Am., Boulder, Colorado, 204, 261-278. https://doi.org/10.1130/2009.1204(12)

Alvarado, P., Christiansen, R., Gregori, D. & Saez, M. (2020). Evidence of site amplification from ground motion of the last two large crustal earthquakes in central-western Argentina. Natural Hazards 102, 1011 – 1031.

Ammirati, J. B., Alvarado, P., & Beck, S. (2015). A lithospheric velocity model for the flat slab region of Argentina from joint inversion of Rayleigh wave phase velocity dispersion and teleseismic receiver functions. *Geophysical Journal International*, *202*(1), 224-241. https://doi.org/10.1093/gji/ggv140

Ammirati, J. B., Venerdini, A., Alcacer, J. M., Alvarado, P., Miranda, S., & Gilbert, H. (2018). New insights on regional tectonics and basement composition beneath the eastern Sierras Pampeanas (Argentine back-arc region) from seismological and gravity data. *Tectonophysics*, *740*, 42-52. https://doi.org/10.1016/j.tecto.2018.05.015

Anderson, R. S., Repka, J. L., & Dick, G. S. (1996). Explicit treatment of inheritance in dating depositional surfaces using in situ ^{10}Be and ^{26}Al. *Geology*, *24*(1), 47-51. https://doi.org/10.1130/0091-7613(1996)024<0047:ETOIID>2.3.CO;2

Anderson, J. G., Wesnousky, S. G., & Stirling, M. W. (1996). Earthquake size as a function of fault slip rate*. Bulletin of the Seismological Society of America*, 86 (3), 683–690.

Anderson, J. G., Biasi, G. P., & Wesnousky, S. G. (2017). Fault-Scaling Relationships Depend on the Average Fault-Slip Rate. *Bulletin of the Seismological Society of America*, 107(6), 2561-2577. https://doi.org/10.1785/0120160361

Armijo, R., Rauld, R., Thiele, R., Vargas, G., Campos, J., Lacassin, R., & Kausel, E. (2010), The West Andean Thrust, the San Ramón Fault, and the seismic hazard for Santiago, Chile. *Tectonics*, 29, TC2007, doi:10.1029/2008TC002427.

Armstrong, P. A., Perez, R., Owen, L. A., & Finkel, R. C. (2010). Timing and controls on late Quaternary landscape development along the eastern Sierra El Mayor range front in northern Baja California, Mexico. *Geomorphology*, *114*(3), 415-430. https://doi.org/10.1016/j.geomorph.2009.08.005

Arriagada, C., Roperch, P., Mpodozis, C., & Cobbold, P. R. (2008), Paleogene building of the Bolivian Orocline: Tectonic restoration of the central Andes in 2-D map view. *Tectonics*, 27, TC6014, doi:10.1029/2008TC002269.

Baby, P., Rochat, P., Mascle, G., & Hérail, G. (1997). Neogene shortening contribution to crustal thickening in the back arc of the Central Andes. *Geology*, 25(10), 883-886. https://doi.org/10.1130/0091-7613(1997)025<0883:NSCTCT>2.3.CO;2

Balco, G., Stone, J. O., Lifton, N. A., & Dunai, T. J. (2008). A complete and easily accessible means of calculating surface exposure ages or erosion rates from ^{10}Be and ^{26}Al measurements. *Quaternary Geochronology*, *3*(3), 174-195. https://doi.org/10.1016/j.quageo.2007.12.001

Balco, G. (2011, December 12). What is a camel diagram anyway? Retrieved July 29, 2020, from https://cosmognosis.wordpress.com/2011/07/25/what-is-a-camel-diagram-anyway/

Bastías, H. (1985). Fallamiento Cuaternario en la región sismotectónica de Precordillera (Doctoral dissertation, Tesis Doctoral. Facultad de Ciencias Exactas, Físicas y Naturales, Universidad Nacional de San Juan), 160 p.

Beck, S., & Zandt, G. (2007). Lithospheric structure and deformation of the flat slab region of Argentina. In: International Federation of Digital Seismograph Network. Data/ Seismic Network, https://doi.org/10.7914/SN/ZL_2007.

Bellahsen, N., Sébrier, M., & Siame, L. (2016). Crustal shortening at the Sierra Pie de Palo(Sierras Pampeanas, Argentina): near-surface basement folding and thrusting. *Geol. Mag.* 153 (5–6), 992–1012. https://doi.org/10.1017/S0016756816000467

Belmont, P., Pazzaglia, F. J., & Gosse, J. C. (2007). Cosmogenic ^{10}Be as a tracer for hillslope and channel sediment dynamics in the Clearwater River, western Washington State. *Earth and Planetary Science Letters*, *264*(1-2), 123-135. https://doi.org/10.1016/j.epsl.2007.09.013

Bierman, P., & Steig, E. J. (1996). Estimating rates of denudation using cosmogenic isotope abundances in sediment. *Earth surface processes and landforms*, *21*(2), 125-139. https://doi.org/10.1016/j.epsl.2007.09.013

Blisniuk, K., Oskin, M., Fletcher, K., Rockwell, T., & Sharp, W. (2012). Assessing the reliability of U-Series and ^{10}Be dating techniques on alluvial fans in the Anza Borrego Desert, California. *Quat. Geochronol.* 13, 26–41. https://doi.org/10.1016/j.quageo.2012.08.004

Bonalumi, A., Martino, R., Baldo, E., Zarco, J., Sfragulla, J., Carignano, C., Kraemer, P.,Escayola, M., Tauber, A., Cabanillas, A., Juri, E., & Torres, B. (1999). Memoria Hojageológica 3166-IV, Villa Dolores. Servicio Geológico Minero Argentino, Buenos Aires.

Borchers, B., Marrero, S., Balco, G., Caffee, M., Goehring, B., Lifton, N., Nishiizumi, K., Phillips, F., Schaefer, J. & Stone, J. (2016). Geological calibration of spallation production rates in the CRONUS-Earth project. Quaternary Geochronology, 31, 188-198.

Brocard, G. Y., Van Der Beek, P. A., Bourlès, D. L., Siame, L. L., & Mugnier, J. L. (2003). Long-term fluvial incision rates and postglacial river relaxation time in the French Western Alps from ^{10}Be dating of alluvial terraces with assessment of

inheritance, soil development and wind ablation effects. *Earth and Planetary Science Letters*, 209(1-2), 197-214. https://doi.org/10.1016/S0012-821X(03)00031-1

Brooks, B., Bevis, M., Smalley, R., Kendrick, E., Manceda, R., Lauría, E., Maturana, R., & Araujo, M. (2003). Crustal motion in the Southern Andes (26°-36°S): Do the Andes behave like a microplate? *Geochemistry, Geophysics, Geosystems*, 4(10),1-14. https://doi.org/10.1029/2003GC000505

Brown, L., Stensland, G. J., Klein, J., & Middleton, R. (1989). Atmospheric deposition of 7Be and ^{10}Be. *Geochimica et Cosmochimica Acta*, *53*(1), 135-142. https://doi.org/10.1016/0016-7037(89)90280-9

Brown, E. T., Edmond, J. M., Raisbeck, G. M., Bourlès, D. L., Yiou, F., & Measures, C. I. (1992). Beryllium isotope geochemistry in tropical river basins. *Geochimica et Cosmochimica Acta*, *56*(4), 1607-1624. https://doi.org/10.1016/0016-7037(92)90228-B

Brown, E. T., Bourlès, D. L., Raisbeck, G. M., Yiou, F., Burchfiel, B.C., Molnar, P., & Qidong, D. (1998). Estimation of slip rates in the southern Tien Shan using cosmic ray exposure dates of abandoned alluvial fans. *Geological Society of America Bulletin*, *110*(3), 377-386. https://doi.org/10.1130/0016-7606(1998)110<0377:EOSRIT>2.3.CO;2

Cahill, T. & Isacks, B. (1992). Seismicity and shape of the subducted Nazca Plate. *Journal of Geophysical Research*, 97(B12), 17503-17529. https://doi.org/10.1029/92JB00493

Candiani, J., Carignano, C., Stuart-Smith, P., Lyons, P., Miró, R., & López, H. (2001). Memoria Hoja Geológica 3166-II, Cruz del Eje. Servicio Geológico Minero Argentino, Buenos Aires.

Carretier, S., Regard, V., Vassallo, R., Aguilar, G., Martinod, J., Riquelme, R., Christophoul, F., Charrier, R., Gayer, E., Farías, M. Audin, L., & Lagane, C. (2015). Differences in ^{10}Be concentrations between river sand, gravel and pebbles along the western side of the central Andes. *Quaternary Geochronology*, 27, 33-51. https://doi.org/10.1016/j.quageo.2014.12.002

Caselli, A., Net, L., Litvak, V., Limarino, C., Poma, S., & Gutierrez, P. (1999). Memoria Hoja Geológica 3166-I. Chamical. Servicio Geológico Minero Argentino, Buenos Aires.

Castellanos, A. (1944). El terremoto de San Juan. En Cuatro lecciones sobre terremotos, Asociación Cultural de Conferencias de Rosario, 79-242.

Chulick, G. S., Detweiler, S., & Mooney, W. D. (2013). Seismic structure of the crust and uppermost mantle of South America and surrounding oceanic basins. *Journal of South American Earth Sciences*, 42, 260-276. https://doi.org/10.1016/j.jsames.2012.06.002

Costa, C. (1999). Tectónica Cuaternaria en las Sierras Pampeanas. En Caminos, R. (ed.) Geología Argentina, SEGEMAR, Anales, 29, 779-784.

Costa, C. (2019). La migración del frente de corrimiento neotectónico de las Sierras Pampeanas y su impronta morfológica. *Revista de la Asociación Geológica Argentina*, 76 (4), 315-325.

Costa, C., Machette, M. N., Dart, R., Bastías, H., Paredes, J. D., Perucca, L. P., Tello, G. E., & Haller, K. M. (2000). Map and database of Quaternary faults and folds in Argentina. *US Geological Survey Open-File Report*, 108, 75.

Costa, C. H., Ahumada, E. A., Gardini, C. E., Vázquez, F. R., & Diederix, H. (2015a). Quaternary shortening at the orogenic front of the Central Andes of Argentina: the Las Penas Thrust System. *Geological Society, London, Special Publications*, 399(1), 245-266. https://doi.org/10.1144/SP399.5

Costa C. H., Ahumada, E. A., Vázquez F. R. & Kröhling D. M. (2015b). Holocene shortening rates of an Andean-front thrust, Southern Precordillera, Argentina. *Tectonophysics*, 664, 191–201. https://doi.org/10.1016/j.tecto.2015.09.017

Costa, C. H., Owen, L. A., Ricci, W. R., Johnson, W. J., & Halperin, A. D. (2018). Holocene activity and seismogenic capability of intraplate thrusts: Insights from the Pampean Ranges, Argentina. *Tectonophysics*, *737*, 57-70. https://doi.org/10.1016/j.tecto.2018.05.002

Costa, C. H., Schoenbohm, L. M., Brooks, B. A., Gardini, C. E., & Richard, A. D. (2019). Assessing Quaternary shortening rates at an Andean frontal thrust (32° 30′S), Argentina. *Tectonics*, 38, 3034– 3051. https://doi.org/10.1029/2019TC005564

D'Arcy, M., Schildgen, T., Turowski, J., & DiNezio, P. (2019). Inferring the timing of abandonment of aggraded alluvial surfaces dated with cosmogenic nuclides. *Earth Surface Dynamics*, 7, 755-771. https://doi.org/10.5194/esurf-7-755-2019

Dühnforth, M., Densmore, A. L., Ivy-Ochs, S., Allen, P., & Kubik, P. W. (2017). Early to Late Pleistocene history of debris-flow fan evolution in western Death Valley (California) using cosmogenic ^{10}Be and ^{26}Al. *Geomorphology*, *281*, 53-65. https://doi.org/10.1016/j.geomorph.2016.12.020

Dunai, T. J. (2010). *Cosmogenic Nuclides: Principles, concepts and applications in the Earth surface sciences*. Cambridge University Press. Cambridge, UK.

Engdahl, E. R., van der Hilst, R., & Buland, R. (1998). Global teleseismic earthquake relocation with improved travel times and procedures for depth determination. *Bulletin of the Seismological Society of America*, 88(3), 722-743.

Engdahl, R., & Villaseñor, A. (2002). Global seismicity: 1900–1999, in International Handbook of Earthquake and Engineering Seismology, Part A, edited by W. H. K. Lee et al, chap. 41, pp. 665–690, Academic, Amsterdam. https://doi.org/10.1016/S0074-6142(02)80244-3.

Fielding, E. J., & Jordan, T. E. (1988). Active deformation at the boundary between the Precordillera and Sierras Pampeanas, Argentina, and comparison with ancient Rocky Mountain deformation. *Geological Society of America Memoirs*, 171, 143-164.

Fosdick, J. C., Carrapa, B., & Ortíz, G. (2015). Faulting and erosion in the Argentine Precordillera during changes in subduction regime: Reconciling bedrock cooling and detrital records. *Earth and Planetary Science Letters*, *432*, 73-83. https://doi.org/10.1016/j.epsl.2015.09.041

Foster, M. A., Anderson, R. S., Gray, H. J., & Mahan, S. A. (2017). Dating of river terraces along Lefthand Creek, western High Plains, Colorado, reveals punctuated incision. *Geomorphology*, 295, 176-190. https://doi.org/10.1016/j.geomorph.2017.04.044

Frankel, K. L., Brantley, K. S., Dolan, J. F., Finkel, R. C., Klinger, R. E., Knott, J. R., Machette, M., Owen, L., Phillips, F. Slate, J. & Wernicke, B. P. (2007). Cosmogenic ^{10}Be and ^{36}Cl geochronology of offset alluvial fans along the northern Death Valley fault zone: Implications for transient strain in the eastern California shear zone. *Journal of Geophysical Research: Solid Earth*, 112(B6). https://doi.org/10.1029/2006JB004350

Furque, G., González, P., & Caballé, M. (1998). Descripción de la hoja geológica 3169-II, San José de Jáchal (Provincias de San Juan y La Rioja). Servicio Geológico y Minero Argentino, Boletín 259, 150 p.

Gans, C. R., Beck, S. L., Zandt, G., Gilbert, H., Alvarado, P., Anderson, M., & Linkimer, L. (2011). Continental and oceanic crustal structure of the Pampean flat slab region, western Argentina, using receiver function analysis: new high-resolution results. *Geophysical Journal International*, *186*(1), 45-58. https://doi.org/10.1111/j.1365-246X.2011.05023.x

García Morabito, E., Terrizzano, C., Zech, R., Yamin, M., Wüthrich, L., Christl, M., Ramos, V., Haghipour, N. & Cortés, J. M. ^{10}Be surface exposure dating reveals unexpected high deformation rates in the central Andean wedge interior. Terra Nova. https://doi.org/10.1111/ter.12487

Gilbert, H. (2008). Lithospheric Structure above the variably dipping Nazca Slab. In: International Federation of Digital Seismograph Networks. Other/Seismic Network, https://doi.org/10.7914/SN/XH_2008

González Bonorino, F. (1950), Algunos problemas geológicos de las Sierras Pampeanas. *Revista de la Asociación Geológica Argentina*, 5, 81-110.

González L, G., Dunai, T., Carrizo, D., & Allmendinger, R. (2006). Young displacements on the Atacama Fault System, northern Chile from field observations and cosmogenic 21Ne concentrations. *Tectonics*, *25*(3), 1-15. https://doi.org/10.1029/2005TC001846

Gosse, J. C., & Phillips, F. M. (2001). Terrestrial in situ cosmogenic nuclides: theory and application. *Quaternary Science Reviews*, 20(14), 1475-1560. https://doi.org/10.1016/S0277-3791(00)00171-2

Groeber, P. (1944). Movimientos tectónicos contemporáneos y un nuevo tipo de dislocaciones. Universidad Nacional de La Plata, Notas del Museo de La Plata, Geología 9, 263-375.

Guerrero, M., Lavandaio, E., & Marcos, O. (1993). Mapa geológico de la provincia de La Rioja escala 1: 500,000. Dirección Nacional del Servicio Geológico, Secretaría de Minería República Argentina.

Gutscher, M. A., Spakman, W., Bijwaard, H., & Engdahl, E. R. (2000). Geodynamics of flat subduction: seismicity and tomographic constraints from the Andean margin. *Tectonics*, 19(5), 814-833. https://doi.org/10.1029/1999TC001152

Gutscher, M. A. (2002). Andean subduction styles and their effect on thermal structure and interplate coupling. *Journal of South American Earth Sciences*, 15(1), 3-10. https://doi.org/10.1016/S0895-9811(02)00002-0

Hancock, G. S., Anderson, R. S., Chadwick, O. A., & Finkel, R. C. (1999). Dating fluvial terraces with ^{10}Be and ^{26}Al profiles: Application to the Wind River, Wyoming. *Geomorphology*, *27*(1-2), 41-60. https://doi.org/10.1016/S0169-555X(98)00089-0

Harrington, H. J. (1948). Volcanes y terremotos. Pleamar, 251.

Hedrick, K., Owen, L.A., Rockwell, T.K., Meigs, A., Costa, C., Caffee, M.W., Masana, E., & Ahumada, E. (2013). Timing and nature of alluvial fan and strath terrace formation in the Eastern Precordillera of Argentina. *Quat. Sci. Rev*. 80, 143-168. https://doi.org/10.1016/j.quascirev.2013.05.004

Instituto Nacional de Prevención Sísmica (INPRES) (1977). Zonificación Sísmica de la República Argentina, Publ. Tec. 5, San Juan, Argentina.

Instituto Nacional de Prevención Sísmica (INPRES) (1982). Microzonificación sísmica del Valle de Tulum, Provincia de San Juan: Resumen ejecutivo, San Juan, Argentina.

Isacks, B. L. (1988). Uplift of the central Andean plateau and bending of the Bolivian orocline. *Journal of Geophysical Research: Solid Earth*, 93(B4), 3211-3231. https://doi.org/10.1029/JB093iB04p03211

Ivy-Ochs, S., Dühnforth, M., Densmore, A. L., & Alfimov, V. (2013). Dating fan deposits with cosmogenic nuclides. In *Dating torrential processes on fans and cones* (pp. 243-263). Springer, Dordrecht.

Jakica, S., Quigley, M. C., Sandiford, M., Clark, D., Fifield, L. K., & Alimanovic, A. (2011). Geomorphic and cosmogenic nuclide constraints on escarpment evolution in

an intraplate setting, Darling Escarpment, Western Australia. *Earth Surface Processes and Landforms*, *36*(4), 449-459. https://doi.org/10.1002/esp.2058

Jones, R. S., Small, D., Cahill, N., Bentley, M. J., & Whitehouse, P. L. (2019). iceTEA: tools for plotting and analysing cosmogenic-nuclide surface-exposure data from former ice margins. *Quaternary Geochronology*, *51*, 72-86. https://doi.org/10.1016/j.quageo.2019.01.001

Jordán, T. E., Isacks, B. L., Allmendinger, R. W., Brewer, J. A., Ramos, V. A., & Ando, C. J. (1983a). Andean tectonics related to geometry of subducted Nazca plate. *Geological Society of America Bulletin*, 94(3), 341-361. https://doi.org/10.1130/0016-7606(1983)94<341:ATRTGO>2.0.CO;2

Jordan, T. E., Isacks, B., Ramos, V. A., & Allmendinger, R. W. (1983b). Mountain building in the Central Andes. Episodes, 557 3, 20-26.

Jordan, T. E., Allmendinger, R. W., Damanti, J. F., & Drake, R. E. (1993). Chronology of motion in a complete thrust belt: the Precordillera, 30-31°S, Andes Mountains. *The Journal of Geology*, 101(2), 135-156.

Jordan, T. E., & Allmendinger, R. W. (1986). The Sierras Pampeanas of Argentina: A modern analogue of Rocky Mountain foreland deformation. *American Journal of Science*, 286(10), 737-764.

Jordan, T. E., & Gardeweg, M. (1989). Tectonic evolution of the late Cenozoic central Andes (20–33°S). The Evolution of the Pacific Ocean Margins, 193-207.

Kadinsky-Cade, K., Reilinger, R., & Isacks, B. (1985). Surface deformation associated with the November 23, 1977, Caucete, Argentina, earthquake sequence. *Journal of Geophysical Research*, 90(B14), 12691-12700. https://doi.org/10.1029/JB090iB14p12691

Kay, S. M., Mpodozis, C., Ramos, V. A., & Munizaga, F. (1991). Magma source variations for mid-late Tertiary magmatic rocks associated with a shallowing subduction zone and a thickening crust in the central Andes (28 to 33 S). *Geological Society of America Special Paper*, *265*, 113-137.

Kendrick, E., Bevis, M., Smalley, R., Cifuentes, O., & Galban, F. (1999). Current rates of convergence across the Central Andes: Estimates from continuous GPS observations. *Geophys. Res. Lett.*, 26, 541–544. https://doi.org/10.1029/1999GL900040

Kendrick, E., Bevis, M., Smalley, R., & Brooks, B. (2001). An integrated crustal velocity field for the central Andes, Geochem. *Geophys. Geosyst.*, 2(11), 1066, doi:10.1029/2001GC000191.

Kendrick, E., Bevis, M., Smalley, R., Brooks, B., Vargas, R. B., Lauria, E., & Fortes, L. P. S. (2003). The Nazca–South America Euler vector and its rate of change. *Journal of South American Earth Sciences*, 16(2), 125-131. https://doi.org/10.1016/S0895-9811(03)00028-2

Kendrick, E., Brooks, B. A., Bevis, M., Smalley, R., Lauria, E., Araujo, M., & Parra, H. (2006). Active orogeny of the South-Central Andes studied with GPS geodesy. *Revista de la Asociación Geológica Argentina*, 61(4), 555-566.

Kley, J., & Monaldi, C. R. (1998). Tectonic shortening and crustal thickness in the Central Andes: How good is the correlation?. *Geology*, 26(8), 723-726. https://doi.org/10.1130/0091-7613(1998)026<0723:TSACTI>2.3.CO;2

Kohl, C. P., & Nishiizumi, K. (1992). Chemical isolation of quartz for measurement of in-situ-produced cosmogenic nuclides. *Geochimica et Cosmochimica Acta*, 56(9), 3583-3587. https://doi.org/10.1016/0016-7037(92)90401-4

Lal, D. (1988). In situ-produced cosmogenic isotopes in terrestrial rocks. *Annual Review of Earth and Planetary Sciences*, 16(1), 355-388. https://doi.org/10.1146/annurev.ea.16.050188.002035

Lal, D. (1991). Cosmic ray labeling of erosion surfaces: in situ nuclide production rates and erosion models. *Earth and Planetary Science Letters*, 104(2-4), 424-439. https://doi.org/10.1016/0012-821X(91)90220-C

Langer, C. J., & Hartzell, S. (1996). Rupture distribution of the 1977 western Argentina earthquake. *Physics of the Earth and Planetary Interiors*, *94*(1-2), 121-132. https://doi.org/10.1016/0031-9201(95)03080-8

Le Dortz, K., Meyer, B., Sébrier, M., Braucher, R., Nazari, H., Benedetti, L., Fattahi, M., Bourlès, D., Foroutan, M., Siame., L., Rashidi, A., & Bateman, M.D. (2011). Dating inset terraces and offset fans along the Dehshir Fault (Iran) combining cosmogenic and OSL methods. *Geophysical Journal International*, 185(3), 1147-1174. https://doi.org/10.1111/j.1365-246X.2011.05010.x

Le Dortz, K., Meyer, B., Sébrier, M., Braucher, R., Bourlès, D., Benedetti, L., Nazari, H., & Foroutan, M. (2012). Interpreting scattered in-situ produced cosmogenic nuclide depth-profile data. *Quaternary Geochronology*, 11, 98-115. https://doi.org/10.1016/j.quageo.2012.02.020

Levina, M., Horton, B. K., Fuentes, F., & Stockli, D. F. (2014). Cenozoic sedimentation and exhumation of the foreland basin system preserved in the Precordillera thrust belt (31–32°S), southern central Andes, Argentina. *Tectonics*, *33*(9), 1659-1680. https://doi.org/10.1002/2013TC003424

Lifton, N., Sato, T., & Dunai, T. J. (2014). Scaling in situ cosmogenic nuclide production rates using analytical approximations to atmospheric cosmic-ray fluxes. *Earth and Planetary Science Letters*, 386, 149-160. https://doi.org/10.1016/j.epsl.2013.10.052

Linkimer, L., Beck, S., Zandt, G., Alvarado, P., Anderson, M., Gilbert, H., & Zhang, H. (2020). Lithospheric structure of the Pampean flat slab region from double-difference tomography. J. S. Am. Earth Sci. 97, 102417. https://doi.org/10.1016/j.jsames.2019.102417.

Lukens, C. E., Riebe, C. S., Sklar, L. S., & Shuster, D. L. (2016). Grain size bias in cosmogenic nuclide studies of stream sediment in steep terrain. *Journal of Geophysical Research: Earth Surface*, *121*(5), 978-999. https://doi.org/10.1002/2016JF003859

Machette, M.N., Slate, J.L., & Phillips, F.M. (2008). Terrestrial cosmogenic-nuclide dating of alluvial fans in Death Valley, California. U.S. Geol. Surv. Prof. Pap. 1755

Matmon, A., Nichols, K., & Finkel, R. (2006). Isotopic insights into smoothening of abandoned fan surfaces, southern California. *Quaternary Research*, *66*(1), 109-118. https://doi.org/10.1016/j.yqres.2006.02.010

Matmon, A., Simhai, O., Amit, R., Haviv, I., Porat, N., McDonald, E.,Benedetti, L., & Finkel, R. (2009). Desert pavement–coated surfaces in extreme deserts present the longest-lived landforms on Earth. *Geological Society of America Bulletin*, 121(5-6), 688-697. https://doi.org/10.1130/B26422.1

McCalpin, J. P. (Ed.). (2009). *Paleoseismology* (Vol. 95). Academic press.

McFadden, L. D., Ritter, J. B., & Wells, S. (1989). Use of multiparameter relative-age methods for age estimation and correlation of alluvial fan surfaces on a desert piedmont, Eastern Mojave Desert, California. *Quat. Res*. 32 (3), 276–290. https://doi.org/10.1016/0033-5894(89)90094-X

Meigs, A., Krugh, W. C., Schiffman, C., Vergés, J., & Ramos, V. A. (2006). Refolding of thin-skinned thrust sheets by active basement-involved thrust faults in the eastern Precordillera of western Argentina. *Revista de la Asociación Geológica Argentina*, 61(4), 589-603.

Mingorance, F. (2006). Morfometría de la escarpa de falla histórica identificada al norte del cerro La Cal, zona de falla La Cal, Mendoza. *Revista de la Asociación Geológica Argentina*, *61*(4), 620-638.

Murphy, B. (2013). A monte Carlo Simulator. https://drive.google.com/file/d/1HU3XIfHUe1yGJ0VSkET3_QZLWLoV_2EZ/view; last accessed July 2020.

Nishiizumi, K., Winterer, E. L., Kohl, C. P., Klein, J., Middleton, R., Lal, D., & Arnold, J. R. (1989). Cosmic ray production rates of ^{10}Be and ^{26}Al in quartz from glacially polished rocks. *Journal of Geophysical Research: Solid Earth*, 94(B12), 17907-17915. https://doi.org/10.1029/JB094iB12p17907

Nur, A., & Ben-Avraham, Z. (1981). Volcanic gaps and the consumption of aseismic ridges in South America. *Memoir of the Geological Society of America*, *154*, 729-740.

Ortiz, G., Alvarado, P., Fosdick, J. C., Perucca, L., Saez, M., & Venerdini, A. (2015). Active deformation in the northern Sierra de Valle Fértil, Sierras Pampeanas,

Argentina. *Journal of South American Earth Sciences*, *64*, 339-350. https://doi.org/10.1016/j.jsames.2015.08.015

Owen, L. A., Frankel, K. L., Knott, J. R., Reynhout, S., Finkel, R. C., Dolan, J. F., & Lee, J. (2011). Beryllium-10 terrestrial cosmogenic nuclide surface exposure dating of Quaternary landforms in Death Valley. *Geomorphology*, *125*(4), 541-557. https://doi.org/10.1016/j.geomorph.2010.10.024

Owen, L.A., Clemmens, S.J., Finkel, R.C., & Gray, H. (2014). Late Quaternary alluvial fans at the eastern end of the San Bernardino Mountains, Southern California. *Quat. Sci. Rev*. 87, 114–134. https://doi.org/10.1016/j.quascirev.2014.01.003

Perarnau, M., Gilbert, H., Alvarado, P., Martino, R., & Anderson, M. (2012). Crustal structure of the Eastern Sierras Pampeanas of Argentina using high frequency local receiver functions. *Tectonophysics*, 580, 208–217. http://dx.doi.org/10.1016/j.tecto.2012.09.021.

Pérez, M., Astorga, A., Monllor, J., & Araujo, M. (1997). Relevamiento planialtimétrico-geológico de la falla Las Chacras, en la quebrada del Barro. In *Octavo Congreso Geológico Chileno: Antofagasta, Chile, Universidad Católica del Norte* (pp. 210-214).

Perucca, L., & Vargas, N. (2014). Neotectónica de la provincia de San Juan, centro-oeste de Argentina. *Boletín De La Sociedad Geológica Mexicana*, 66(2), 291-304.

Pilger, R. H. (1984). Cenozoic plate kinematics, subduction and magmatism: South American Andes. *Journal of the Geological Society*, 141(5), 793-802. https://doi.org/10.1144/gsjgs.141.5.0793

Portenga, E. W., & Bierman, P. R. (2011). Understanding Earth's eroding surface with 10 Be. *GSA today*, 21(8), 4-10. https://doi.org/10.1130/G111A.1

Portner, D. E., Beck, S., Zandt, G., & Scire, A. (2017). The nature of subslab slow velocity anomalies beneath South America. *Geophysical Research Letters*, *44*(10), 4747-4755. https://doi.org/10.1002/2017GL073106

Proyecto Multinacional Andino (PMA): Geociencia para las Comunidades Andinas (2008). Atlas de deformaciones cuaternarias de los Andes. Servicio Nacional de Geología y Minería, Publicación Geológica Multinacional, 7, 1-320, 1 mapa en CD-ROM.

Ragona, D., Anselmi, G., Gonzalez, P., & Vujovich, G. (1995). Mapa geológico de la provincial de San Juan escala 1: 500,000. Dirección Nacional del Servicio Geológico, Secretaría de Minería República Argentina.

Ramos, V. A. (1988). The tectonics of the Central Andes; 30 to 33°S latitude. *Geological Society of America Special Papers*, 218, 31-54.

Ramos, V.A. (1994). Terranes of southern Gondwanaland and their control in the Andean structure (30-33_S lat.). In: Reutter, K.J., Scheuber, E., Wigger, P.J. (Eds.), Tectonics of the Southern Central Andes, Structure and Evolution of an Active Continental Margin. Springer, Berlin, Germany, 249-261.

Ramos, V. (1999). Plate tectonic setting of the Andean Cordillera. *Episodes*, 22, 183-190.

Ramos, V. A., Cegarra, M., & Cristallini, E. (1996). Cenozoic tectonics of the High Andes of west-central Argentina (30–36°S latitude). *Tectonophysics,* 259(1), 185-200. https://doi.org/10.1016/0040-1951(95)00064-X

Ramos, V.A., Cegarra, M., Lo Forte, G. & Cominguez, A. (1997). El frente orogénico en la Sierra de Pedernal (San Juan, Argentina): su migración a través de los depósitos orogénicos. 8o Congreso Geológico Chileno, Actas, 3, 1709-1713.

Ramos, V. A., Dallmeyer, R. D., & Vujovich, G. (1998). Time constraints on the early Palaeozoic docking of the Precordillera, central Argentina. Geological Society, London, Special Publications, 142(1), 143–158. https://doi.org/10.1144/GSL.SP.1998.142.01.08

Ramos, V.A., & Vujovich, G.I. (2000). Hoja geológica 3169-IV San Juan, Provincia de San Juan. Servicio Geológico Minero Argentino.

Ramos, V. A., Cristallini, E. O., & Pérez, D. J. (2002). The Pampean flat-slab of the Central Andes. *Journal of South American Earth Sciences*, 15(1), 59-78. https://doi.org/10.1016/S0895-9811(02)00006-8

Ramos, V. A., Zapata, T., Cristallini, E., & Introcaso, A. (2004). The Andean thrust system—Latitudinal variations in structural styles and orogenic shortening, in Thrust Tectonics and Hydrocarbon Systems, edited by K. R. McClay, AAPG Mem., 82, 30–50.

Ramos, V. A., & Folguera, A. (2009). Andean flat-slab subduction through time. *Geological Society, London, Special Publications*, 327(1), 31-54. https://doi.org/10.1144/SP327.3

Ramos, V.A. & Vujovich, G.I. (2000). Hoja Geológica 3169-IV, San Juan, Provincia de San Juan. Subsec. Minería Nación, Servicio Geológico Minero Argentino, Buenos Aires, Boletín 243, p. 82.

Repka, J. L., Anderson, R. S., & Finkel, R. C. (1997). Cosmogenic dating of fluvial terraces, Fremont River, Utah. *Earth and Planetary Science Letters*, *152*(1-4), 59-73. https://doi.org/10.1016/S0012-821X(97)00149-0

Richardson, T., Ridgway, K. D., Gilbert, H., Martino, R., Enkelmann, E., Anderson, M., & Alvarado, P. (2013). Neogene and Quaternary tectonics of the Eastern Sierras Pampeanas, Argentina: Active intraplate deformation inboard of flat-slab subduction. *Tectonics*, *32*(3), 780-796. https://doi.org/10.1002/tect.20054

Riesner, M., Lacassin, R., Simoes, M., Carrizo, D., & Armijo, R. (2018). Revisiting the crustal structure and kinematics of the Central Andes at 33.5°S: Implications for the mechanics of Andean mountain building. *Tectonics*, 37, 1347–1375. https://doi.org/10.1002/2017TC004513

Riihimaki, C. A., Anderson, R. S., Safran, E. B., Dethier, D. P., Finkel, R. C., & Bierman, P. R. (2006). Longevity and progressive abandonment of the Rocky Flats surface, Front Range, Colorado. *Geomorphology*, *78*(3-4), 265-278. https://doi.org/10.1016/j.geomorph.2006.01.035

Rimando, J. M., & Schoenbohm, L. M. (2020). Regional relative tectonic activity of structures in the Pampean flat slab segment of Argentina from 30 to 32°S. *Geomorphology*, 350, 106908. https://doi:10.1016/j.geomorph.2019.106908

Rimando, J. M., Schoenbohm, L. M., Costa, C. H., Owen, L. A., Cesta, J. M., Richard, A. D., & Gardini, C. E. (2019). Late Quaternary Activity of the La Rinconada Fault Zone, San Juan, Argentina. *Tectonics*, 38(3), 916-940. https://doi.org/10.1029/2018TC005321.

Ritz, J., Vassallo, R., Brakcher, R., Brown, E. T., Carretier, S., & Bourlès, D. L. (2006). Using in situ-produced^ 1^ 1Be to quantify active tectonics in the Gurvan Bogd mountain range (Gobi-Altay, Mongolia). *Special Papers-Geological Society of America*, *415*, 87.

Rockwell, T. K., Ragona, D. E., Meigs, A. J., Owen, L. A., Costa, C. H., & Ahumada, E. A. (2014). Inferring a Thrust-Related Earthquake History from Secondary Faulting: A Long Rupture Record of La Laja Fault, San Juan, Argentina. *Bulletin of the Seismological Society of America*, 1, 269–284. https://doi.org/10.1785/0120110080

Rossello, E. A., & Mozetic, M. E. (1999). Caracterización estructural y significado geotectónico de los depocentros cretácicos continentales del centro-oeste argentino. *Boletim do 5º Simpósio o Cretáceo do Brasil*, *107*, 13.

Rothis, L. M., Perucca, L. P., Malnis, P. S., Zuñiga, A. P., Alcacer, J. M., Haro, F. M., & Vargas, N. (2018). Análisis morfotectónico en el piedemonte suroccidental del antepais andino, Sierras Pampeanas Occidentales, San Juan, Argentina. *Geosciences= Geociências*, *37*(1), 55-74.

Rothis, L. M., Perucca, L. P., Malnis, P. S., Alcacer, J. M., Haro, F. M., & Vargas, H. N. (2019). Neotectonic, morphotectonic and paleoseismologic analysis of the Las Chacras Fault System, Sierras Pampeanas Occidentales, San Juan, Argentina. *Journal of South American Earth Sciences*, *91*, 144-153. https://doi.org/10.1016/j.jsames.2019.02.001

Salomon, E., Schmidt, S., Hetzel, R., Mingorance, F., & Hampel, A. (2013). Repeated folding during late Holocene earthquakes on the La Cal thrust fault near Mendoza city (Argentina). *Bulletin of the Seismological Society of America*, 103(2A), 936-949. https://doi.org/10.1785/0120110335

Schepers, G., van Hinsbergen, D. J. J., Spakman, W., Kosters,M. E., Boschman, L. M., & McQuarrie, N. (2017). South-American plate advance and forced Andean trench retreat as drivers for transient flat subduction episodes. *Nature Communications*, 8, 15249. https://doi.org/10.1038/ ncomms15249

Schmidt, C. J., Astini, R. A., Costa, C. H., Gardini, C. E., & Kraemer, P. E. Cretaceous Rifting, Alluvial Fan Sedimentation, and Neogene Inversion, Southern Sierras Pampeanas, Argentina, in Petroleum Basins of South America, vol. 62, AAPG Memoir, pp. 341 – 358, Tulsa, 1995.

Schmidt, S., Hetzel, R., Mingorance, F., & Ramos, V. A. (2011a). Coseismic displacements and Holocene slip rates for two active thrust faults at the mountain front of the Andean Precordillera (~33°S). *Tectonics*, 30, TC5011. https://doi.org/10.1029/2011TC002932

Schmidt, S., Hetzel, R., Kuhlmann, J., Mingorance, F., & Ramos, V. A. (2011b). A note of caution on the use of boulders for exposure dating of depositional surfaces. *Earth and Planetary Science Letters*, *302*(1-2), 60-70. https://doi.org/10.1016/j.epsl.2010.11.039

Siame, L. L., Bourlès, D. L., Sébrier, M., Bellier, O., Castano, J. C., Araujo, M., Perez, M., Raisbeck, G., & Yiou, F. (1997). Cosmogenic dating ranging from 20 to 700 ka of a series of alluvial fan surfaces affected by the El Tigre fault, Argentina. *Geology*, 25(11), 975-978. https://doi.org/10.1130/0091-7613(1997)025<0975:CDRFTK>2.3.CO;2

Siame, L. L., Bellier, O., Sébrier, M., Bourlès, D. L., Leturmy, P., Perez, M., & Araujo, M. (2002). Seismic hazard reappraisal from combined structural geology, geomorphology and cosmic ray exposure dating analyses: The Eastern Precordillera thrust system (NW Argentina). *Geophysical Journal International*, 150(1), 241-260. https://doi.org/10.1046/j.1365-246X.2002.01701.x

Siame, L. L., Bellier, O., Sébrier, M., & Araujo, M. (2005). Deformation partitioning in flat subduction setting: Case of the Andean foreland of western Argentina (28°S–33°S). *Tectonics*, 24, TC5003, doi:10.1029/ 2005TC001787.

Siame, L., Bellier, O., Sébrier, M. (2006). Active tectonics in the Argentine Precordillera and Western Sierras Pampeanas. *Rev. Asoc. Geol. Arg*., 61 (4), 604-619.

Siame, L. L., Sébrier, M., Bellier, O., Bourlès, D., Costa, C., Ahumada, E. A., Gardini, C., & Cisneros, H. (2015). Active basement uplift of Sierra Pie de Palo (Northwestern Argentina): Rates and inception from ^{10}Be cosmogenic nuclide concentrations. *Tectonics*, 34(6), 1129-1153. https://doi.org/10.1002/2014TC003771

Smalley, R., & Isacks, B. L. (1990). Seismotectonics of thin-and thick-skinned deformation in the Andean Foreland from local network data: Evidence for a seismogenic lower crust. *Journal of Geophysical Research: Solid Earth*, 95(B8), 12487-12498. https://doi.org/10.1029/JB095iB08p12487

Smalley, R., Pujol, J., Regnier, M., Chiu, J. M., Chatelain, J. L., Isacks, B. L., Araujo, M., & Puebla, N. (1993). Basement seismicity beneath the Andean Precordillera thin-skinned thrust belt and implications for crustal and lithospheric behavior. *Tectonics*, 12(1), 63-76. https://doi.org/10.1029/92TC01108

Snyder, D. B., Ramos, V. A., & Allmendinger, R. W. (1990). Thick-skinned deformation observed on deep seismic reflection profiles in western Argentina. *Tectonics*, *9*(4), 773-788. https://doi.org/10.1029/TC009i004p00773

Stein, S. (2007), Approaches to continental intraplate earthquake issues, in Continental Intraplate Earthquakes: Science, Hazard, and Policy Issues, edited by S. Stein and S. Mazzotti. *Geol. Soc. of Am. Spec. Pap*., 425, 1– 16.

Stone J. (2000). Air pressure and cosmogenic isotope production. *J. Geophys. Res.* 105: 23753-23759. https://doi.org/10.1029/2000JB900181

Stone, J. O. (2001). Extraction of Al & Be from quartz for isotopic analysis. University of Washington Cosmogenic Isotope Laboratory website. https://depts.washington.edu/cosmolab/chem/Al-26_Be-10.pdf

Tranel, L. M., & Strow, M. L. (2017). ^{10}Be analysis of amalgamated talus pebbles to investigate alpine erosion, Garnet Canyon, Teton Range, Wyoming. *Geosphere*, *13*(1), 36-48. https://doi.org/10.1130/GES01297.1

Uliana, M.A., Biddle, K.T., Cerdan, J. (1989). Mesozoic extension and the formation of Argentine sedimentary basins. A.J. Tankard, H.R. Balkwill (Eds.), Extensional Tectonics and Stratigraphy of the North Atlantic Margins, *Am. Assoc. Pet. Geol. Mem.*, 46, 599-614.

Uliarte, E., Bastías, H., & Ruzycki, L. (1987). Morfología y neotectónica en el Cerro La Chilca, Pedernal, Provincia de San Juan, Argentina. 10° Congr Geol Argent Tucuman, Actas, 1, 227-230.

U.S. Geological Survey (USGS) (2021). M 6.4 - 28 km SW of Pocito, Argentina. https://earthquake.usgs.gov/earthquakes/eventpage/us7000d18q/moment-tensor. Accessed: 26 Feb 2021.

van Dongen, R., Scherler, D., Wittmann, H., & von Blanckenburg, F. (2019). Cosmogenic ^{10}Be in river sediment: where grain size matters and why. *Earth Surface Dynamics*, 7, 393-410. https://doi.org/10.5194/esurf-7-393-2019

Vergés, J., Ramos, V. A., Meigs, A., Cristallini, E., Bettini, F. H. & Cortés, J. M. (2007). Crustal wedging triggering recent deformation in the Andean thrust front between 31°S and 33°S: Sierras Pampeanas-Precordillera interaction. *J. Geophys. Res.*, 112, B03S15. doi:10.1029/2006JB004287.

Volponi, F., Quiroga, M., Robles, A., & Sisterna, J. (1984). El terremoto de Caucete del 23 de noviembre de 1977, Instituto Sismológico Zonda, FCEFyN, Universidad Nacional de San Juan, San Juan, 97 pp.

Vujovich, G., Chernicoff, J., Tchiliguirian, P., Godeas, M., Marín, G., Pezzutti, N., & Sepúlveda, E. (1998). Hoja geológica 3166-III, Chepes, provincias de San Juan y La Rioja. Servicio Geológico Minero Argentino.

Wells, D. L., & Coppersmith, K. J. (1994). New empirical relationships among magnitude, rupture length, rupture width, rupture area, and surface displacement. *Bulletin of the seismological Society of America*, *84*(4), 974-1002.

Yáñez, G. A., Ranero, C. R., von Huene, R., & Díaz, J. (2001). Magnetic anomaly interpretation across the southern central Andes (32–34°S): The role of the Juan Fernández Ridge in the late Tertiary evolution of the margin. *Journal of Geophysical Research: Solid Earth*, *106*(B4), 6325-6345. https://doi.org/10.1029/2000JB900337

Yang, X., Li, W., & Qin, Z. (2015). Calculation of reverse-fault-related parameters using topographic profiles and fault bedding. *Geodesy and Geodynamics*, 6(2), 106-112. https://doi.org/10.1016/j.geog.2014.09.002

Zapata, T. R., & Allmendinger, R. W. (1996). Thrust-front zone of the Precordillera, Argentina: a thick-skinned triangle zone. *AAPG bulletin*, 80(3), 359-381. https://doi.org/10.1306/64ED87E6-1724-11D7-8645000102C1865D